RSC Sustainability

ROYAL SOCIETY OF CHEMISTRY

PAPER

View Article Online
View Journal | View Issue

Cite this: *RSC Sustainability*, 2025, **3**, 3582

Nyctanthes arbor-tristis L. mediated sustainable synthesis of α-Fe_2O_3/g-C_3N_4 S-scheme heterojunctions for enhanced photocatalytic degradation of tetracycline hydrochloride: a mechanistic insight and DFT study†

Mano Ranjan Barik,[a] Jagadish Kumar [b] and Sushanta Kumar Badamali *[a]

The development of efficient and sustainable photocatalytic systems is critical for addressing emerging pollutants in wastewater. In this study, we report the green synthesis of a novel S-scheme α-Fe_2O_3/g-C_3N_4 heterojunction, engineered to enhance the visible-light-driven photodegradation of tetracycline hydrochloride (TCH). The composite was fabricated using an eco-friendly route involving *Nyctanthes arbor-tristis* L. leaf extract, ensuring a minimal environmental footprint. Structural and chemical characterization studies *via* XRD and FTIR confirmed the presence of distinct crystalline phases and key functional groups, including Fe–O and C=N bonds. Morphological analysis using FESEM and HRTEM revealed a well-defined interfacial architecture, while XPS confirmed the presence of Fe^{3+}, C, and N elements, validating successful heterojunction formation. The heterostructure exhibited a BET surface area of 21 m^2 g^{-1} and a narrowed optical band gap of 2.2 eV, using UV-Vis DRS. Photoluminescence (PL) spectroscopy demonstrated significantly reduced recombination of photogenerated electron–hole pairs, indicating efficient charge separation. Under visible-light irradiation, the α-Fe_2O_3/g-C_3N_4 photocatalyst achieved an impressive 93% degradation of TCH within 60 minutes, significantly outperforming pristine g-C_3N_4(32%) and α-Fe_2O_3(43%). The enhanced photocatalytic activity is attributed to a synergistic S-scheme charge transfer pathway that promotes redox potential and suppresses charge recombination. A detailed parametric study was conducted to evaluate the effects of catalyst dosage, initial TCH concentration, heterojunction ratio, and exposure duration. DFT calculations explained the geometrically favorable crystal and band structures. Superoxide radicals were identified as major reactive species from scavenging studies. A plausible mechanism for TCH degradation was established based on LCMS analysis.

Received 15th June 2025
Accepted 23rd June 2025

DOI: 10.1039/d5su00437c

rsc.li/rscsus

Sustainability spotlight

This study presents a green and sustainable approach for designing an advanced S-scheme α-Fe_2O_3/g-C_3N_4 heterojunction photocatalyst leveraging the phytochemical richness of *Nyctanthes arbor-tristis* L. leaf extract. Employing an eco-friendly synthesis route, the work eliminates the need for hazardous chemicals, promoting sustainable material fabrication. The photocatalyst efficiently degrades tetracycline hydrochloride, a persistent pharmaceutical pollutant, under visible light, offering a cost-effective and scalable protocol for wastewater treatment. Mechanistic insights, supported by DFT calculations, highlight the enhanced charge transfer efficiency of the heterojunction. Our work aligns with UN Sustainable Development Goals: SDG 6 (Clean Water and Sanitation), SDG 12 (Responsible Consumption and Production), and SDG 13 (Climate Action) by promoting green synthesis for wastewater treatment, reducing chemical waste, and supporting sustainable environmental practices.

1 Introduction

The surge in population growth and escalating environmental pollution have elevated the concentration of hazardous pollutants in the environment, posing significant risks to public health. The rapid expansion and extensive utilization of pharmaceuticals have led to the contamination of aquatic systems with complex organic pollutants.[1] Among the commonly consumed antibiotics, tetracycline hydrochloride (TCH) is a widely used broad-spectrum antibiotic, frequently employed to prevent infections in humans and animals. A significant portion of TCH is not metabolized by animals; hence, large quantities of the drug or its metabolites are directly discharged through excretion into different water streams.[2] These residues

[a]*Department of Chemistry, Utkal University, Vani Vihar, Bhubaneswar-751004, Odisha, India. E-mail: skbuche@utkaluniversity.ac.in*

[b]*Department of Physics, Utkal University, Vani Vihar, Bhubaneswar-751004, Odisha, India*

† Electronic supplementary information (ESI) available. See DOI: https://doi.org/10.1039/d5su00437c

pose substantial environmental and health risks by contaminating aquatic ecosystems through the growth of multi-resistant microorganisms. According to the notification released by the Ministry of Environment, Forest and Climate Change, India (New Delhi, 23rd January 2020), the tolerance limit of the TCH drug is about 0.4 ppm. The persistent nature of such pollutants underscores the urgent need for efficient and sustainable remediation strategies.

Nevertheless, different methods such as precipitation, solvent extraction, adsorption, froth flotation, coagulation, oxidation, evaporation, sedimentation, ion exchange, and advanced oxidation processes (AOPs) have been used to eliminate antibiotics from contaminated water.[3] Nevertheless, some of these methods are often time-consuming, expensive, and involve additional chemicals, which are eventually polluting the environment. In a major breakthrough in 1972, Honda and Fujishima reported photo-electrochemical water splitting using a TiO_2 catalyst, which shifted focus to photocatalytic reactions using semiconductor materials.[4,5] Since then, semiconductor-mediated photocatalysis has been extensively studied as it utilizes renewable energy and fewer chemicals, making it a more sustainable option to address the removal of organic contaminants.

Over the period, several studies have been reported on heterogeneous photocatalysis using materials such as TiO_2, ZnO, Fe_2O_3, CdS, ZnS, MoO_3, g-C_3N_4, and GO towards the removal of a wide range of organic pollutants from various contaminated water streams.[6–9] However, the practical use of individual semiconductor photocatalysts encounters certain challenges, including poor electrical conductivity, fast recombination of photogenerated electron–hole pairs, susceptibility to photo corrosion, poor absorption of solar energy, leaching, *etc.*[10,11]

Hence, the development of photocatalysts needs to overcome the above facts apart from possessing light absorption in the visible region and robust redox capability. A narrow bandgap is necessary to capture a broader spectrum of solar light, while a wider bandgap is preferable to effectively facilitate photocatalytic reactions.[12] The requirements to obtain maximum redox ability and broad light absorption are thus in contradiction with one another. As a result, the creation of a heterojunction, achieved by combining two semiconductors in direct contact, is a valuable architecture to reduce the challenges faced by bare semiconductors.[13]

Recent studies on heterojunction structures have proven their ability to effectively separate photogenerated electron–hole pairs and integrate the advantages of each semiconductor involved. These are typically formed by combining two semiconducting materials with a staggered band structure arrangement, which supports the Type-II photocatalytic mechanism.[14] This arrangement enhances the efficiency of photocatalytic reactions by optimizing charge carrier separation and migration. Two types of heterojunctions, namely Z- and S-scheme, have recently been studied. The Z-scheme is relatively complex and often involves additional cocatalysts or intricate charge transfer processes, which can reduce its efficiency in large-scale applications. To overcome these disadvantages, Yu *et al.* reported an S-scheme (step-scheme) heterojunction, consisting of two types of photocatalysts, an oxidation photocatalyst (OP) and a reduction photocatalyst (RP).[15] In which the OP is positioned at a higher potential, whereas the RP is positioned at a lower potential. In such a system, less redox potential electrons in the CB of the oxidation photocatalyst and holes in the VB of the reduction photocatalyst tend to recombine through an electric field formed at the interface. However, the useful electrons and holes on the other side are effectively separated to participate in the degradation process.[16,17] In brief, the S-scheme heterojunction is often considered superior to the Z-scheme in photocatalytic applications owing to its more efficient charge carrier separation, better stability, and simpler design. Importantly, in an S-scheme-based photocatalyst, the holes and electrons are more effectively separated and directed to the appropriate reaction sites, minimizing recombination and improving photocatalytic efficiency. The S-scheme typically requires fewer components and a simpler band alignment between semiconductors, making it easier and cost-effective with the possibility of realistic applications.[18,19]

It is worth mentioning that the combination of α-Fe_2O_3 and g-C_3N_4 constitutes an important heterojunction photocatalyst, and the relevant features of α-Fe_2O_3 and g-C_3N_4 are outlined below. Fe_2O_3 is an excellent semiconducting material with good photocatalytic activity. α-Fe_2O_3 possesses a relatively low bandgap of approximately 1.8 eV, corresponding to an absorption wavelength of around 600 nm.[20] This reduced bandgap allows it to effectively absorb visible light from the solar spectrum, enhancing its utility in various photocatalytic applications owing to its availability, potent oxidizing capacity, excellent chemical stability, low cost, and environmental friendliness. Similarly, graphitic carbon nitride (g-C_3N_4), a two-dimensional polymeric material, has gained remarkable attention as a catalyst with a bandgap of ~2.7 eV.[21–24] The sp^2-hybridized carbon framework enhances electron mobility, while the layered structure provides an expanded surface area, thereby improving its photocatalytic performance. This material is also valued for its non-toxic characteristics, cost-effectiveness, and simple synthesis process.

Various synthetic techniques have been utilized to fabricate nanostructured α-Fe_2O_3 with g-C_3N_4.[25] Among all, the hydrothermal technique offers advantages such as mild reaction conditions, moderate operational complexity, and better crystalline products.[26] However, this process often involves the use of templates and expensive chemicals, which can pose environmental concerns. To overcome these drawbacks, alternative green synthesis approaches have been developed utilizing naturally occurring green plants.[27] These environmentally benign methods are cost-effective, provide high yields, and exhibit good reproducibility. Several herbs and plants occurring in nature are rich sources of antioxidants, including terpenoids, flavonoids, ketones, aldehydes, and amide compounds, which are available in their roots, stems, and leaves. The extracts from these plants are widely recognized for their eco-friendly, sustainable, and biocompatible properties in the nanoparticle synthesis process.[28,29]

Table 1 Comparative studies on the photodegradation of tetracycline using various photocatalysts

Entry	Catalyst	Catalyst (g L^{-1})	Tetracycline (mg L^{-1})	Source; duration; pH	Degradation, %	Ref.
1	$BiFeO_3/TiO_2$	1.0	10	Vis/3 h/5	72	30
2	Bi/α-Bi_2O_3/g-C_3N_4	1.0	10	Vis/3 h	91	31
3	γ-Fe_2O_3/g-C_3N_4	0.5	10	Vis/2 h	74	32
4	$CuInS_2$/g-C_3N_4	1.0	10	Vis/1 h	84	33
5	$CuBi_2O_4$/g-C_3N_4	0.5	10	Vis/1 h	90	34
6	$CdIn_2S_4$/g-C_3N_4	1.0	10	Vis/2 h	80	35
7	Nb_2O_5/g-C_3N_4	1.0	20	Sunlight/2.5 h	90	36
8	α-MnO_2/B@g-C_3N_4	1.0	10	Vis/1.3 h	87	37
9	Bi_2O_4 @SnS	1.0	10	Vis/2 h/7	91	38
10	WO_3/Bi_2O_4	0.2	10	Vis/2 h/5	90	39
11	g-$C_3N_4/ZnFe_2O_4/Ag_2CO_3$	0.2	20	Vis/2 h	84	40
12	$MnFe_2O_4$/ZIF-8	0.5	05	Vis/1.5 h/9	95	41
13	$Mn_{0.3}Cd_{0.7}S/FeNi_8$-LDH	0.5	50	Vis/0.5	72	42
14	g-C_3N_4/BiOCl	1.0	20	Vis/2 h/7	89	43
15	α-Fe_2O_3/g-C_3N_4	0.5	20	Vis/1 h/5	93	Present work

Concentrating our attention on TCH degradation through photocatalysis by varying different parameters such as reaction conditions, catalyst, source of light, pH, *etc.*, available in the reported literature is summarized in Table 1. Some of the listed studies require closer inspection due to their effectiveness. Chen *et al.* reported a notable advancement in photocatalysis with their Bi_2O_3/g-C_3N_4 heterojunction, enhanced by incorporating plasmonic metallic Bi and strategically introduced oxygen vacancies. However, this composite achieved a degradation of 91% within a very large reaction duration of 3 h.[31] Similarly, Hong *et al.* demonstrated the efficacy of an expensive metal oxide, Nb_2O_5 modified g-C_3N_4 photocatalyst, which exhibited remarkable stability and efficiency in the mineralization of TCH, attaining 90% mineralization within 2.5 h under sunlight irradiation.[36] Zhao *et al.* introduced an advanced 2D/1D S-scheme heterojunction Bi_2O_4@SnS and achieved 91% degradation of tetracycline hydrochloride.[38] Here, the catalyst dose (1 g L^{-1}) and reaction time (2 h) are relatively high. In analogous studies, Jiang *et al.*[39] and Azqandi *et al.*[41] reported commendable photocatalytic efficiencies of 90% and 95% under visible light irradiation. Despite these notable advancements, the predominant challenges remain the relatively extended reaction times, expensive metals, and the inherent complexity associated with these catalysts. An ideal photocatalyst should be cost-effective, abundant, and sustainable while ensuring minimal atom utilization. It must operate efficiently under visible or solar radiation, eliminating the need for multicomponent systems. Furthermore, it should require only minimal catalyst dosage and reaction time for optimal performance.

This study aims to develop a sustainable, green synthesis route for fabricating α-Fe_2O_3/g-C_3N_4 heterojunctions using naturally occurring green leaf extracts of *Nyctanthes arbortristis L.* It is a commonly available plant with a very high quantity of phytochemicals in its leaves, which can play a vital role in the development of nanomaterials. By leveraging cost-effective α-Fe_2O_3 and carbon-based g-C_3N_4, which efficiently absorb visible light, the research focuses on enhancing photocatalytic degradation of tetracycline hydrochloride (TCH) through an S-scheme charge transfer mechanism. Comprehensive characterization is conducted to explain the structural, electronic, and charge transfer properties of the heterojunctions. Density Functional Theory (DFT) calculations further optimize the structure and band alignment of individual components. Additionally, the study evaluates the durability and recyclability of the photocatalyst to assess its potential for sustainable wastewater treatment, advancing environmentally friendly approaches to pollutant remediation.

2 Experimental

2.1 Reagents and catalysts

All precursors utilized in the studies were of analytical grade and used without any additional purification. Tetracycline hydrochloride capsule I.P. 500 mg was purchased from Abbott India Limited. Iron(III) nitrate nonahydrate (>98%), urea (99.5%), and ethanol (99.9%) were purchased from Sisco Research Laboratories (SRL) Pvt. Ltd. Deionized water was used as the reaction medium throughout the photocatalytic degradation studies.

2.2 Preparation of g-C_3N_4 sheets from urea

In a typical synthetic method, 15 g of urea was placed directly into a 50 mL crucible and subjected to calcination in a muffle furnace.[44] The crucible was partially sealed and heated at 550 °C for 3 h at a heating rate of 5 °C min^{-1} (Scheme 1a and b). After cooling to room temperature, the obtained yellowish powder was treated sequentially with 1 M hydrochloric acid and deionized water to eliminate ammonia residues from the sample surface. The powders were then filtered and dried in an air oven at 80 °C for 6 h. The dried powders were heated at 400 °C for 3 h to remove ammonium salts that may have formed during acid treatment. This process yielded the final sheet-like g-C_3N_4.

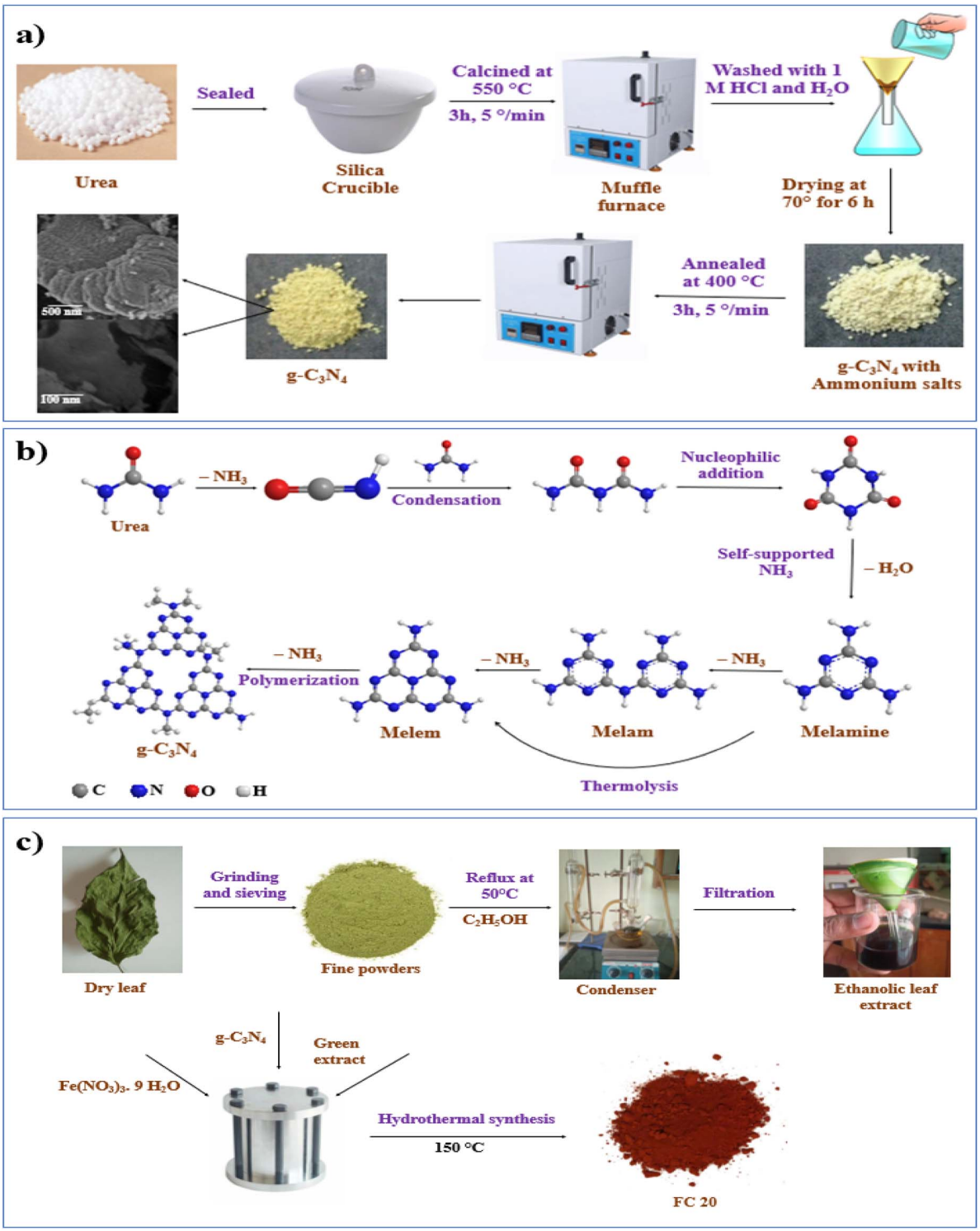

Scheme 1 Graphical representation of catalyst fabrication. (a) Preparation of g-C_3N_4; (b) mechanism of g-C_3N_4 formation; (c) preparation of α-Fe_2O_3/g-C_3N_4 heterojunction.

2.3 Preparation of *Nyctanthes arbor-tristis* leaf extract

Fresh and healthy *Nyctanthes arbor-tristis* leaves were collected from the Utkal University campus, Bhubaneswar, India (geographical location: latitude 20.300622° and longitude 85.842409°). The leaves were carefully washed to remove adsorbed dust from the surface and then air-dried at room temperature for around 15 days. The dried leaves were cut into small pieces, ground, and finally sieved to obtain a fine powder. As presented in Scheme 1c, two grams of this powder were taken with 100 mL of ethanol and subjected to extraction under reflux conditions at 50 °C for 5 h. The resulting ethanolic green extract was filtered and used immediately.

2.4 Green synthesis of S-scheme α-Fe_2O_3/g-C_3N_4 heterojunctions

In a typical synthesis procedure, a specified amount of g-C_3N_4 was dispersed into 25 mL of deionized water, followed by the addition of 20 mL of *Nyctanthes* leaf extract to the reaction mixture. The resulting mixture was subjected to sonication for 1 h. After this step, a precalculated amount of $Fe(NO_3)_3 \cdot 9H_2O$ was dissolved in the above solution and placed under sonication for another 30 min at room temperature. After sonication was completed, the mixture was transferred into a 100 mL Teflon-lined stainless-steel autoclave and placed under hydrothermal aging at 150 °C for 10 h. After the crystallization, the product was filtered off using Whatman No. 1 filter paper, washed repeatedly with deionized water and ethanol to discard any remaining impurities, and finally dried at 80 °C for 6 h. The product was annealed at 400 °C for 4 h to eliminate any remaining phytochemicals from the surface. Different weight-to-weight ratios of g-C_3N_4 and α-Fe_2O_3 were prepared and designated as FC10 (10% of g-C_3N_4 and 90% of α-Fe_2O_3), FC20 (20% of g-C_3N_4 and 80% of α-Fe_2O_3), FC30 (30% of g-C_3N_4 and 70% of α-Fe_2O_3), FC 80 (80% of g-C_3N_4 and 20% of α-Fe_2O_3), and FC 90 (90% of g-C_3N_4 and 10% of α-Fe_2O_3). Additionally, green α-Fe_2O_3 was prepared following the same procedure without the addition of g-C_3N_4 for a comparative assessment of α-Fe_2O_3 activity.

2.5 Characterization

The catalyst was characterized systematically to understand the structural, elemental, electronic, optical, and morphological properties. Structural properties of α-Fe_2O_3/g-C_3N_4 were studied by an X-ray diffraction technique using a PANanalytical diffractometer in Bragg–Brentano geometry with monochromatic Cu-Kα ($\lambda = 1.54$ Å) radiation. A field emission scanning electron microscope was used to obtain the morphology of the catalyst using a Zeiss machine operating at 5 kV. Before analysis, the sample was prepared by gold sputter-coating (metallization) to enhance conductivity. The crystallographic structure of the heterojunction at an atomic scale was obtained by a high-resolution transmission electron microscope (PHILIPS CM 200) operating at an accelerating voltage of 200 kV. Before analysis, the powder sample was ultrasonicated in ethanol, followed by deposition on a carbon-coated copper grid and dried overnight. For atomic force microscopy analysis, the powder sample was dried overnight at 70 °C, and pellets were prepared using a hydraulic press. Then the images were captured using the MFP-3D Origin Model (Oxford Instruments, USA). The presence of functional groups in the sample was investigated by using a Fourier transform infrared spectrophotometer (Shimadzu) employing KBr as a reference material. Raman spectral analysis was carried out in a LabRAM HR Evolution Raman Spectrometer. The surface area, pore volume, and pore size measurements of FC 20 were carried out using a Quantachrome machine. The samples were outgassed at 180 °C for 8 h before N_2 adsorption–desorption measurement. The thermal stability of the samples was analyzed using DTA-TGA equipment (STA-6000, PerkinElmer, Germany) in the temperature range of 30 to 900 °C. The X-ray photoelectron spectroscopy data were collected using an Omicron ESCA machine (Oxford Instrument, Germany). It was performed on powder samples mounted on Cu tape and degassed overnight in the FEL chamber under high vacuum (5.2×10^{-10} mbar) to minimize surface contamination. A monochromatic Al Kα source (1486.7 eV) was used, with energy resolution confirmed by a FWHM of 0.60 eV. The average particle size in the colloidal state, as well as the surface charge of catalysts, was probed using a particle size zeta potential analyser (Malvern Panalytical) instrument. The diffusion reflectance UV vis data were collected by using a PerkinElmer spectrophotometer (Lambda 365+) using $BaSO_4$ as a standard. Photoluminescence spectra were recorded on an Edinburgh FLS 980S photoluminescence spectrometer at an excitation wavelength of 330 nm using a xenon lamp as an excitation source. The liquid chromatography mass spectrometry patterns were collected by using the Agilent 6530 Q-TOF LCMS system. Density functional theory (DFT) calculations were performed using the QUANTUM ESPRESSO package.

2.6 Photocatalytic reactor and degradation studies

Photocatalytic degradation studies were carried out using a custom-built vertically mounted reactor system (manufactured by LELESIL, India) with a working capacity ranging from 25 to 300 mL.[45] In a standard experiment, 100 mL of TCH solution (20 mg L^{-1}) was combined with 50 mg of photocatalyst and stirred in the dark for 30 min to allow the system to reach adsorption–desorption equilibrium on the catalyst surface. After the equilibrium, the suspension was subjected to visible light exposure to facilitate photocatalytic degradation. At specified intervals, 5 mL aliquots of the reaction mixture were taken out and centrifuged for 10 min to isolate the catalyst. The degradation of TCH was assessed by measuring the fall in absorbance maxima at 357 nm using an Agilent Cary 200 UV-Vis spectrophotometer (USA).[46] The catalyst amount and TCH concentration were varied to optimize the reaction conditions and obtain the maximum efficiency.

In all the reactions, the degree of TCH degradation was calculated by using formula (1):

$$\text{Degradation } (\%) = \frac{C_0 - C_t}{C_0} \times 100 \quad (1)$$

where C_0 and C_t represent the TCH concentrations at the initial time and at a certain time interval, t, respectively.

To identify the degraded components, the reaction aliquots were centrifuged and separated from the catalyst. Subsequently, the liquid chromatography mass spectrometry (LCMS) analysis of the filtrate was conducted to characterize the degradation product/pathways.

3 Results and discussion

3.1 XRD analysis

The XRD pattern of the α-Fe_2O_3/g-C_3N_4 heterostructure reveals characteristic peaks from both components, reflecting their distinct crystallographic presence in the heterostructure

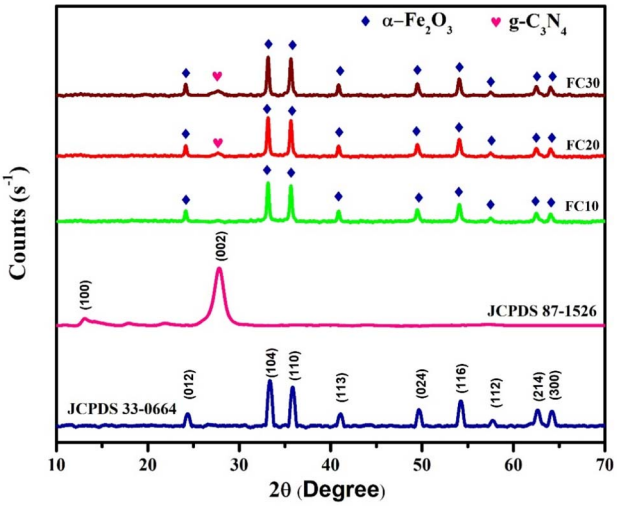

Fig. 1 XRD spectra of prepared photocatalysts.

(Fig. 1). For α-Fe_2O_3 (hematite, JCPDS 33-0664), prominent peaks are observed around 24.39°, 33.34°, 35.85°, 41.11°, 49.65°, 54.17°, 57.71°, 62.67°, and 64.26° (2θ), corresponding to the planes (012), (104), (110), (113), (024), (116), (112), (214), and (300), respectively, of the hexagonal structure.[47] Similarly, g-C_3N_4 showed a characteristic peak around 27.4°, associated with its layered structure (JCPDS 33-0664).[48] The heterostructure α-Fe_2O_3/g-C_3N_4 showed retention of both components without the formation of any new phases.

3.2 FESEM analysis

The FESEM images of the α-Fe_2O_3/g-C_3N_4 catalyst are shown in Fig. 2, and they provide important insights into the morphological and structural characteristics of the material. The α-Fe_2O_3 nanoparticles are observed as two spherical nanoparticles elongated (Fig. 2a), having an average particle size of ~50–60 nm. The FESEM images of g-C_3N_4 reveal its characteristic open layered structure, consisting of two-dimensional sheet-like morphologies (Fig. 2b). Fig. 2(c) illustrates the α-Fe_2O_3/g-C_3N_4 heterostructure, where spherical α-Fe_2O_3 nanoparticles are seen evenly distributed across the g-C_3N_4 surface. Furthermore, the elemental mapping confirmed the presence of Fe, O, N, and C, demonstrating the successful incorporation of both components. This uniform dispersion plays a vital role in ensuring maximum exposure of the active sites along with facilitating efficient charge transfer, which is desirable for improved catalytic performance.

3.3 HRTEM studies

The High Resolution Transmission Electron Microscopy images presented in Fig. 3 provide a detailed morphological and structural analysis of FC 20. Fig. 3(a) depicts the overall morphology with agglomerated nanoparticles in the nanoscale structure of the composite. Fig. 3(b) and (c) provides a clearer view of the spherical α-Fe_2O_3 nanoparticles, emphasizing their uniform size distribution and intimate contact with the g-C_3N_4 surface, which promotes potential interfacial interactions.

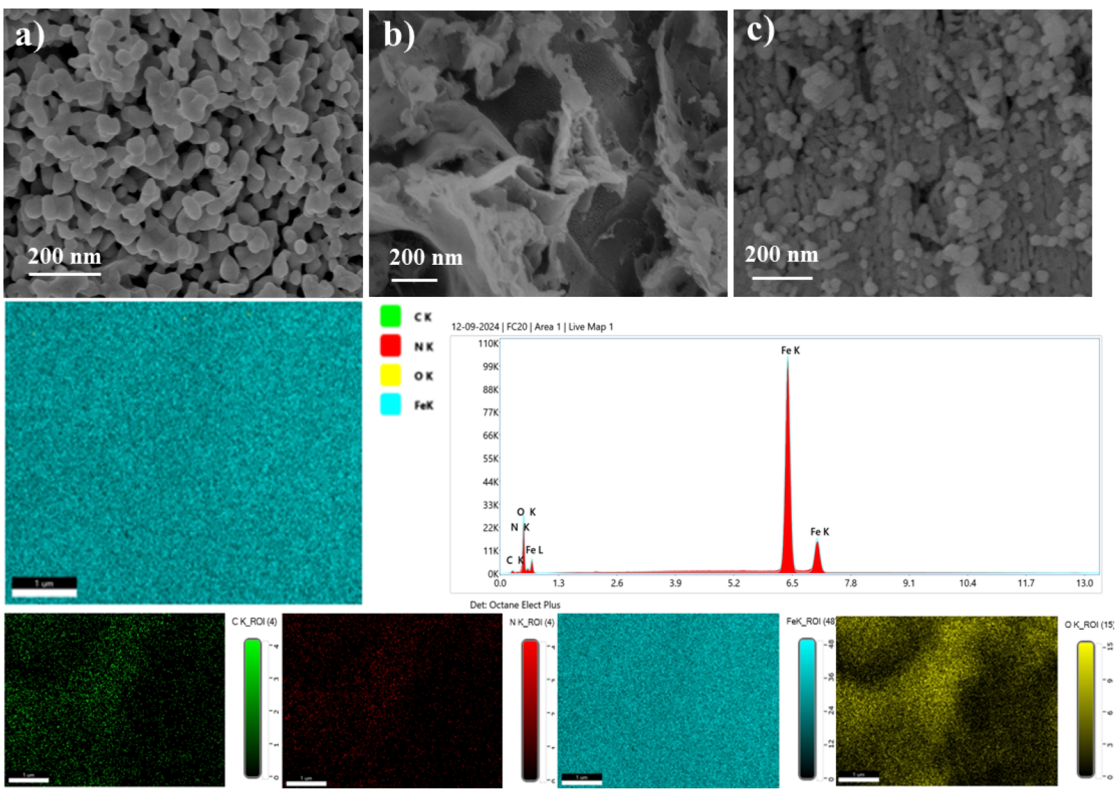

Fig. 2 FESEM images of α-Fe_2O_3 (a), g-C_3N_4 (b), and FC 20 (c); EDAX pattern and elemental mapping of FC 20.

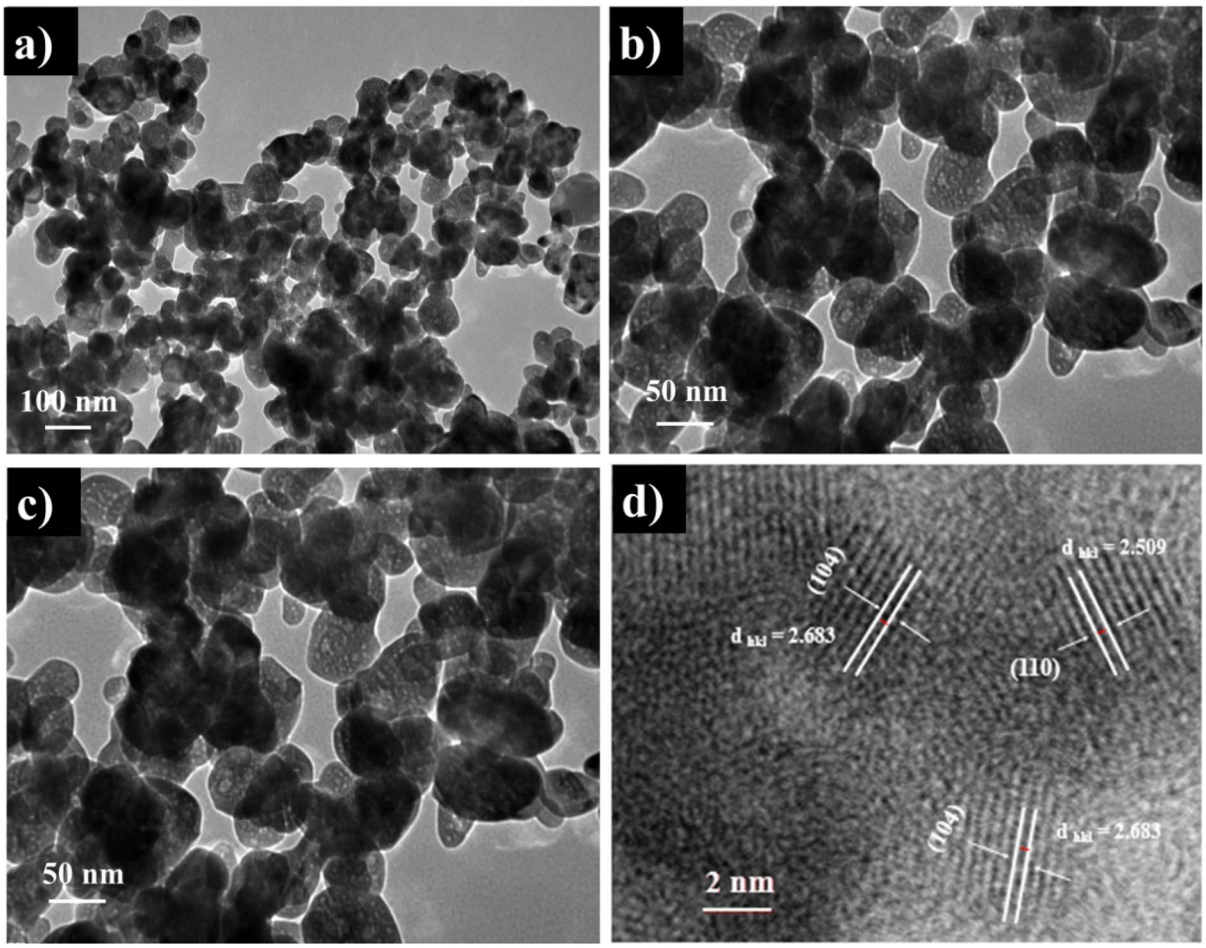

Fig. 3 HRTEM images of FC 20.

Fig. 3(d) displays a high-resolution lattice fringe analysis of FC 20. Distinct lattice fringes corresponding to interplanar distances, such as 2.5 and 2.6 Å for the (110) plane and (104) reflection, respectively, are observed, matching the crystal structure of α-Fe_2O_3. These HRTEM images collectively demonstrate the successful integration of α-Fe_2O_3 nanoparticles with g-C_3N_4.

3.4 FTIR and Raman studies

FTIR spectroscopy was performed to investigate the structural and chemical characteristics of α-Fe_2O_3, g-C_3N_4, and their composite, as presented in Fig. 4(a). The FTIR spectrum of α-Fe_2O_3 exhibits significant absorption bands, notably the O–H stretching vibrations at approximately 3200–3600 cm^{-1}, indicative of surface hydroxyl groups, and Fe–O stretching modes within the range of 450–700 cm^{-1}, characteristic of the hematite framework. In contrast, g-C_3N_4 displays distinct absorption features, including the C=N stretching vibrations centered around 1640 cm^{-1}, C–N stretching modes between 1000 and 1200 cm^{-1}, and the breathing mode of the triazine unit peak near 800 cm^{-1}.[48] The composite FC 20 spectrum shows peaks from both constituents, which suggests the successful assembly of the two materials. This evidence for the preservation of characteristic functional groups highlights the structural integrity of the composite material.

The Raman spectrum of the α-Fe_2O_3/g-C_3N_4 composite provides valuable information about the structural and vibrational properties of the material (Fig. 4b). In the spectrum, characteristic peaks of α-Fe_2O_3 are observed in the range of 200–650 cm^{-1}, corresponding to vibrational modes of Fe–O bonds, such as symmetric stretching (E_g) and asymmetric bending (A_{1g}) at 287, 410, and 607 cm^{-1} and 221 and 498 cm^{-1}, respectively.[49] These peaks confirm the crystalline nature of hematite. For g-C_3N_4, the Raman spectrum typically shows bands at ~480, ~708, and ~980 cm^{-1}. The peak at ~708 cm^{-1} represents the *s*-triazine ring.[50] In the composite, the presence of characteristic peaks of both α-Fe_2O_3 and g-C_3N_4 is retained, confirming the successful amalgamation.

3.5 N_2 adsorption–desorption and TGA analysis

Nitrogen adsorption–desorption analysis is extensively used to assess the textural characteristics of materials, including surface area, pore volume, and pore size distribution, and the N_2 adsorption–desorption isotherm is shown in Fig. 4(c). The specific surface area of FC 20 was determined to be 21 m^2 g^{-1} using the Brunauer–Emmett–Teller (BET) method. The total

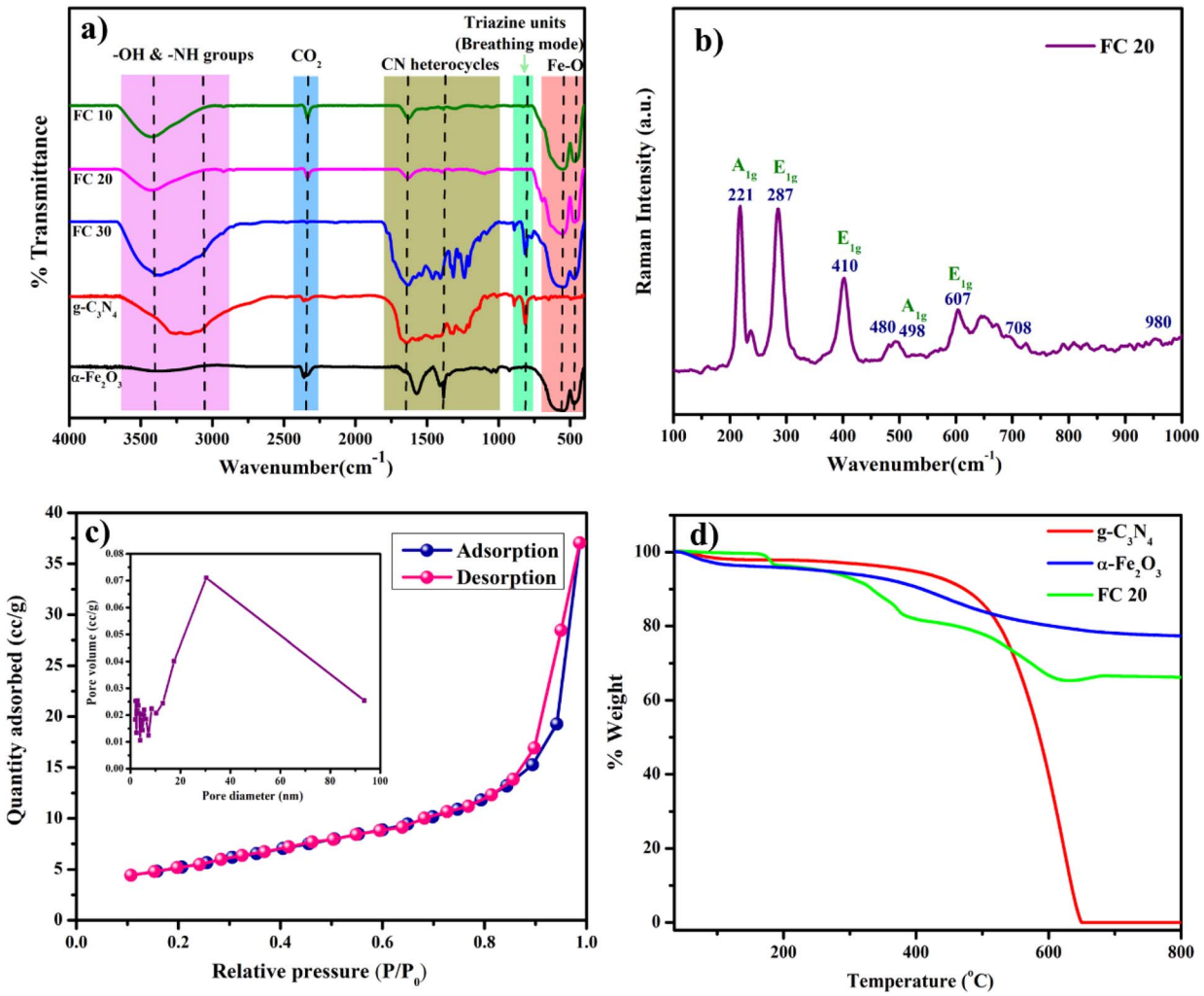

Fig. 4 FTIR spectra (a), Raman spectra (b), BET surface area analysis (c), and TGA plot of FC 20 (d).

pore volume was measured to be 0.059 cm^3 g^{-1}, while the average pore diameter was 2.1 nm. The pore size distribution is quite broad, which reveals a highly open structure. The adsorption branch of the isotherm represents nitrogen gas uptake at increasing relative pressures, while the desorption branch reflects the release of nitrogen during pressure reduction. The isotherm typically exhibits a hysteresis loop, which occurs due to capillary condensation in meso–macropores.

The thermogravimetric analysis (TGA) of α-Fe_2O_3, g-C_3N_4, and FC 20 is presented in Fig. 4(d). It provides crucial information on their thermal stability and decomposition behavior. For pure α-Fe_2O_3, the TGA plot typically shows ~6% weight loss due to physisorbed water molecules in the region of 80–100 °C. The subsequent weight loss of ~15–20% in the region of 300–600 °C is due to the removal of residual carbon content, which was possibly retained due to the green synthesis process. In contrast, g-C_3N_4 exhibits significant weight loss between 500 and 650 °C, corresponding to the thermal decomposition of the carbon nitride framework. For FC 20, the TGA curve combines features of both components, with an initial minor weight loss at lower temperatures due to adsorbed water or surface-bound volatiles, followed by a prominent weight loss in the temperature zone of 300–400 °C associated with the residual carbon residues. A significant weight loss was also noted between 500 and 650 °C, which can be attributed to the thermal decomposition of g-C_3N_4. The thermal behavior of the composite validates the effective integration of g-C_3N_4 with α-Fe_2O_3, as trailing occurred in the region of 500–550 °C, compared to individual components. The residual weight at higher temperatures corresponds to the stable α-Fe_2O_3 content. This analysis highlights the potential of the composite for high-temperature applications.

3.6 XPS analysis

X-ray Photoelectron Spectroscopy (XPS) is a highly sensitive technique that provides information about the elemental composition and oxidation states of the elements present in the material. The XPS spectra of FC 20 (Fig. 5) display characteristic peaks for iron (Fe) at binding energies ~710 eV (Fe $2p_3/_2$) and 724 eV (Fe $2p_1/_2$), confirming the presence of Fe^{3+} in the α-Fe_2O_3 lattice.[51] Peaks around 530 eV indicate oxygen and possible

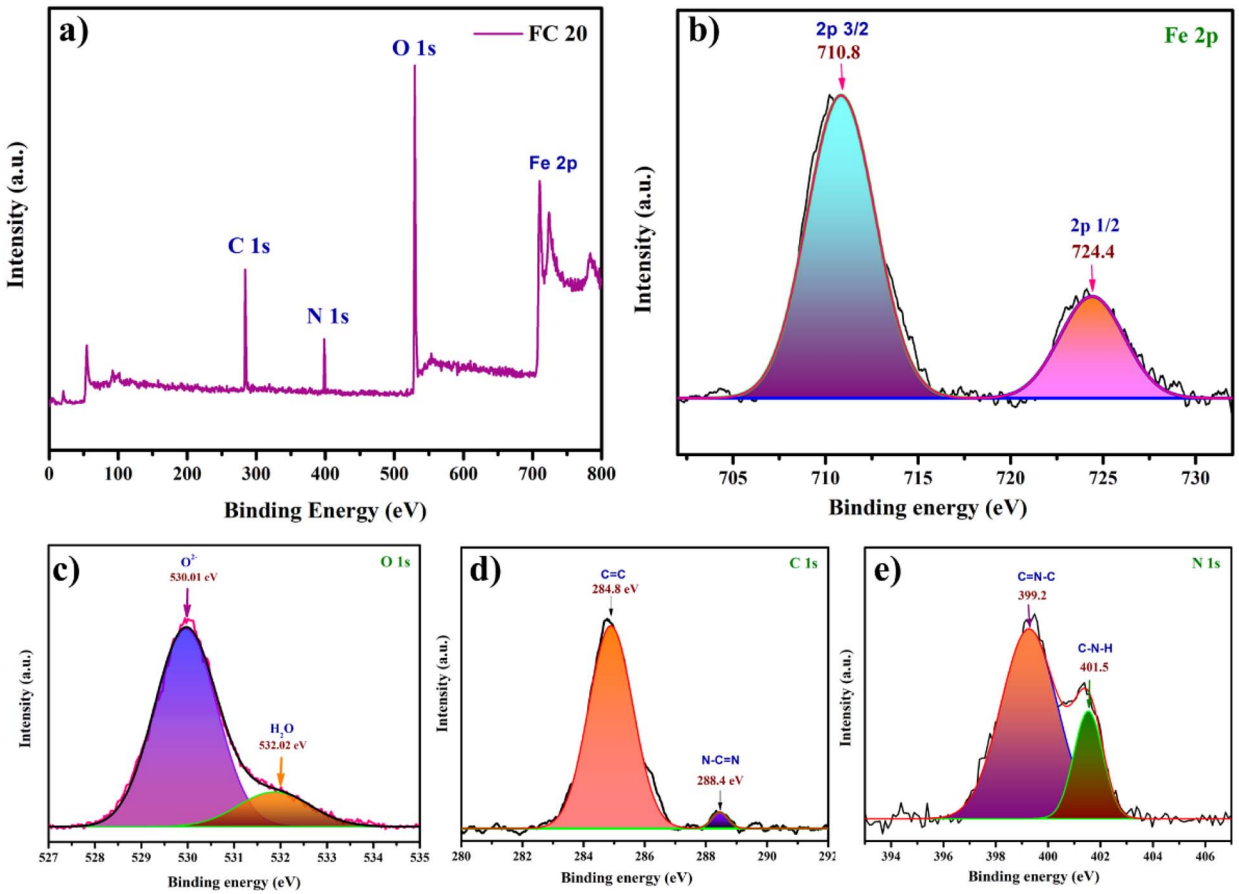

Fig. 5 XPS survey of FC 20 (a), and high-resolution binding spectra of Fe 2p (b), O 1s (c), C 1s (d), and N 1s (e).

hydroxyl groups in the heterojunction. Furthermore, peaks for carbon (C 1s at 284 eV) and nitrogen (N 1s at 400 eV) highlight the contribution of g-C_3N_4, indicating its role in electronic properties and stability. This precise information regarding the electronic nature is often essential in explaining the activities.

3.7 UV-vis DRS and photoluminescence studies

The UV-Vis diffuse reflectance spectroscopy spectra of α-Fe_2O_3, g-C_3N_4, and their heterojunction are presented in Fig. 6(a), which reveal distinct optical properties that are crucial for photocatalytic applications. α-Fe_2O_3 displays a characteristic broad absorption spectrum between 250 and 550 nm, with a bandgap of ~1.8 eV (Fig. S2, ESI†), indicating effective light harvesting for photocatalytic reactions. Likewise, g-C_3N_4 is also an efficient photocatalyst under visible light, and shows less broader absorption spectrum between 250 and 430 nm with a bandgap around 2.7 eV (Fig. S2, ESI†), enabling it to utilize solar light effectively. FC 20 exhibits a synergistic effect and a band gap of 2.26 eV, indicating enhanced light harvesting across a broader spectral range (Fig. 6b). This improvement is attributed to the effective charge separation and transfer phenomena due to the heterojunction formation between α-Fe_2O_3 and g-C_3N_4, optimizing photocatalytic efficiency.

The photoluminescence (PL) spectra of g-C_3N_4, α-Fe_2O_3, and composite FC 20 are presented in Fig. (c) and (d), which provide valuable insights into their charge carrier dynamics and recombination behaviors. α-Fe_2O_3 and g-C_3N_4 exhibit strong emission peaks, due to the recombination of electron–hole pairs, indicating relatively inefficient charge separation. In contrast, the FC 20 heterostructure demonstrates a significant reduction in PL intensity compared to α-Fe_2O_3, indicating enhanced charge separation and transfer between the components. This reduction in PL intensity signifies the effective suppression of charge recombination due to the formation of a heterojunction, which promotes the migration of charge carriers toward the surface for catalytic reactions. Overall, the comparative analysis of the PL spectra of different composites is carried out, and FC 20 showed enhanced charge separation and reduced recombination losses.

3.8 Computational study

The electronic properties of the S-scheme α-Fe_2O_3/g-C_3N_4 catalyst were thoroughly investigated, adopting first-principles calculations based on density functional theory (DFT) using the QUANTUM ESPRESSO package.[52] All calculations were conducted by using the plane-wave pseudopotential method with generalized gradient approximation (GGA) employing the Perdew–Burke–Ernzerhof (PBE) exchange–correlation function.[53,54] Ultrasoft pseudopotentials were used, where the valence electrons are 3d, 3p, 3s, and 4s for Fe, and 2s and 2p for

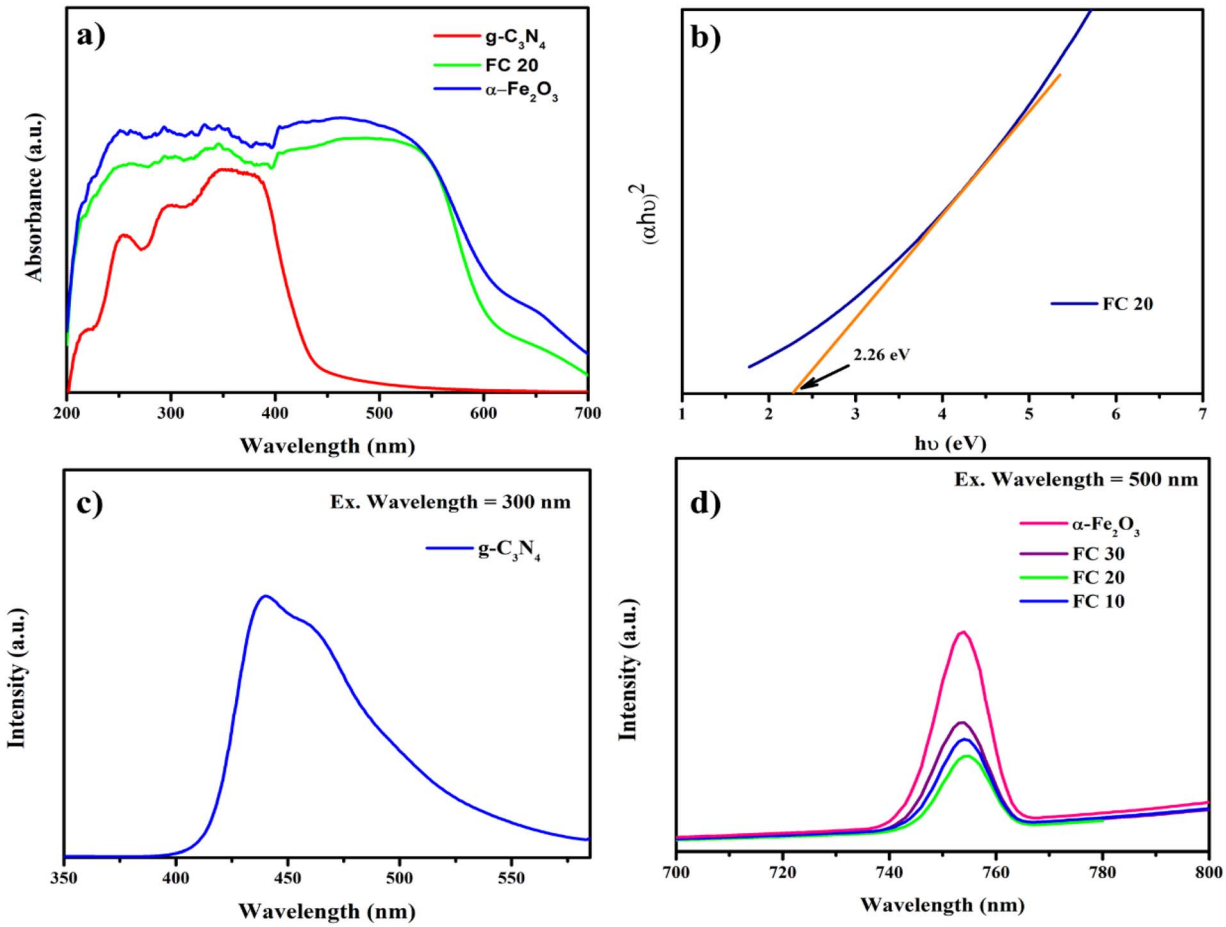

Fig. 6 UV-Vis DRS spectra of α-Fe_2O_3, g-C_3N_4, and FC 20 (a), Tauc plot of FC 20 (b), and PL spectra of g-C_3N_4 (c), α-Fe_2O_3, and heterostructures (d).

O, N, and C.[47] A well-converged kinetic energy cutoff 350Ry and an appropriate *k*-point mesh were employed for computational accuracy, with a convergence threshold of 10^{-7}.[55] Structural optimization was carried out prior to electronic property calculations to obtain the stable configurations of α-Fe_2O_3, g-C_3N_4, and the α-Fe_2O_3/g-C_3N_4 heterostructure, and the optimized structures are presented in Fig. 7.[56–60] This optimization step ensured that the geometries used in subsequent computations were energetically favorable, thereby improving the accuracy of the charge density, PDOS, and band structure results.

We have analyzed the charge density distribution, projected density of states (PDOS), and band structure of the α-Fe_2O_3/g-C_3N_4 material. The iso-electronic contour plot captures the valence electron charge density map in a particular plane and is presented in Fig. 8. The PDOS analysis revealed the distinct contributions of different atomic orbitals to the electronic states near the Fermi level. The g-C_3N_4 component exhibited dominant contributions from C-2p and N-2p orbitals, while significant Fe-3d and O-2p state electrons characterized α-Fe_2O_3. The combined α-Fe_2O_3/g-C_3N_4 system showed strong orbital interaction, reinforcing efficient charge transport mechanisms and minimizing charge recombination (Fig. 9).

The computed band structure further elucidated the electronic properties of the system and the band gap values of 1.695, 0.00, and 0.247 eV for g-C_3N_4, α-Fe_2O_3, and α-Fe_2O_3/g-C_3N_4, respectively, which were calculated at the ground state and within the limitations of DFT. The individual band structures of g-C_3N_4 demonstrated the intrinsic semiconducting nature, with a bandgap favoring visible light absorption. In the heterostructure, band alignment was observed to facilitate charge transfer *via* an S-scheme mechanism, which enhances redox reactions and contributes to superior photocatalytic performance. Thus, computational results provide theoretical support for the improved photocatalytic activity of the S-scheme α-Fe_2O_3/g-C_3N_4 heterostructure, reinforcing its potential for environmental applications.

3.9 Photocatalytic degradation of TCH

The electronic spectra of TCH in aqueous solution show an absorption band between 210 and 375 nm, with a characteristic λ_{max} value of 357 nm. This band arises primarily from n → π* and π → π* electronic transitions, attributed to π-conjugated structures and the presence of heteroatoms in the molecule. The λ_{max} at 357 nm is considered to be the signature to identify and quantify TCH in the reaction mixture. When TCH was

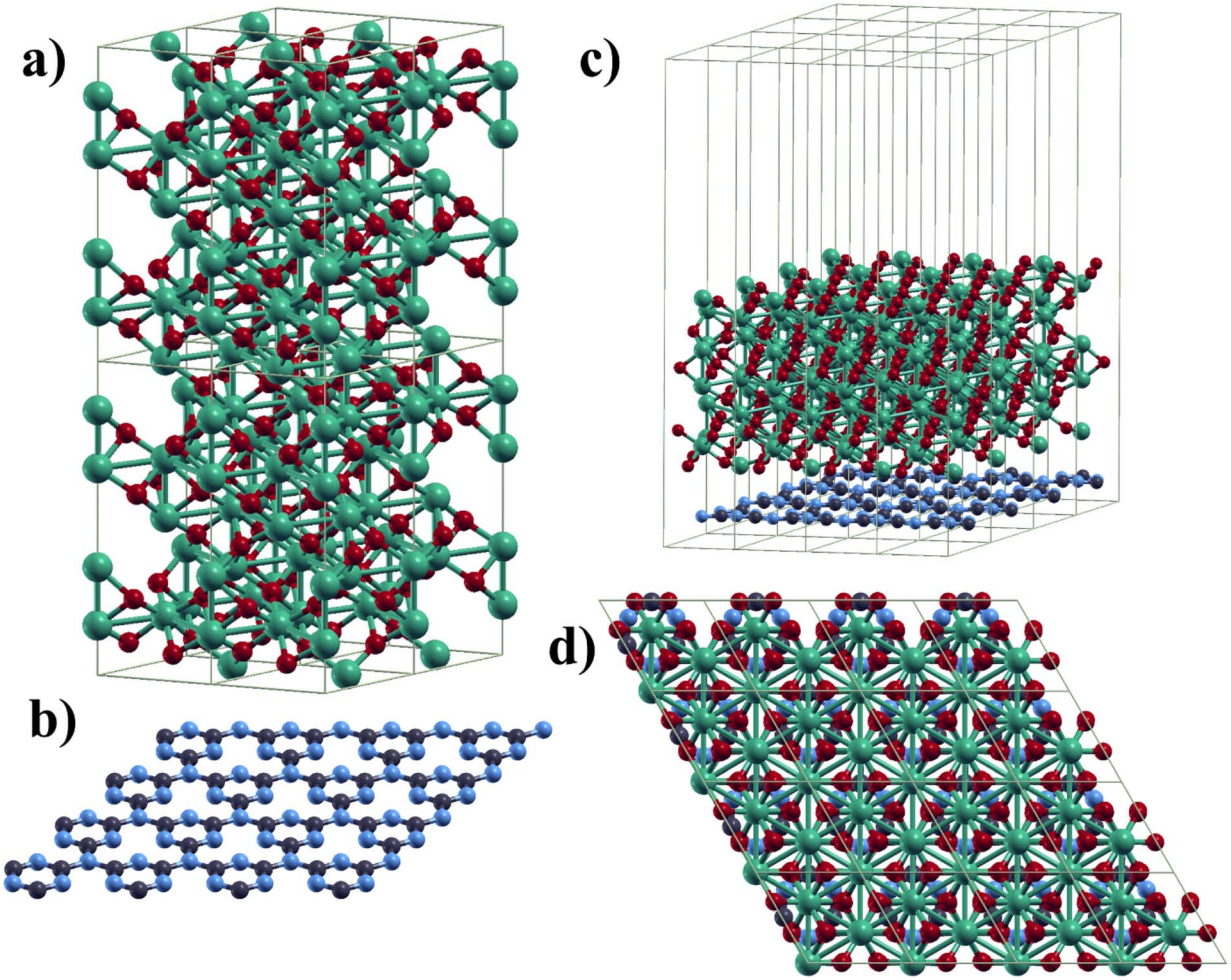

Fig. 7 Optimized structures of α-Fe_2O_3 (a), g-C_3N_4 (b), and α-Fe_2O_3/g-C_3N_4 (c and d).

placed in the dark, either with or without contact with the catalyst, negligible degradation (<1%) occurred. However, exposure to visible light for an hour, in the absence of the catalyst, led to approximately 5% degradation, possibly due to photolysis. The catalytic performance of α-Fe_2O_3, g-C_3N_4, and α-Fe_2O_3/g-C_3N_4 was studied under visible light (Fig. 10a). Among the heterojunctions, *i.e.*, FC 30, FC 20, and FC 10, FC 20 demonstrated the highest degradation efficiency of TCH, achieving a maximum degradation of ~93%. In contrast, the individual components exhibited significantly lower efficiencies, *i.e.*, α-Fe_2O_3 and g-C_3N_4 yield only 43 and 32% degradation, respectively. The enhanced photocatalytic performance of FC 20 was also substantiated by the PL data, demonstrating decreased hole–electron pair recombination due to the S-scheme mechanism. A comparative experiment in which the α-Fe_2O_3/g-C_3N_4 heterojunction was synthesized under identical conditions but without the use of the leaf extract showed degradation efficiency of 82% (Fig.S3, ESI†). The decreased degradation efficiency is attributed to the differences in morphology, crystallinity, and particle size (Fig. S4, ESI†),

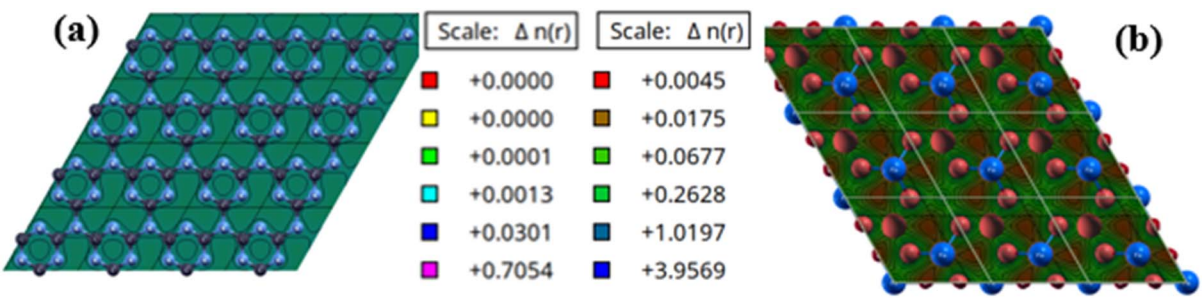

Fig. 8 The valence electron charge density map of g-C_3N_4 (a) and α-Fe_2O_3 (b).

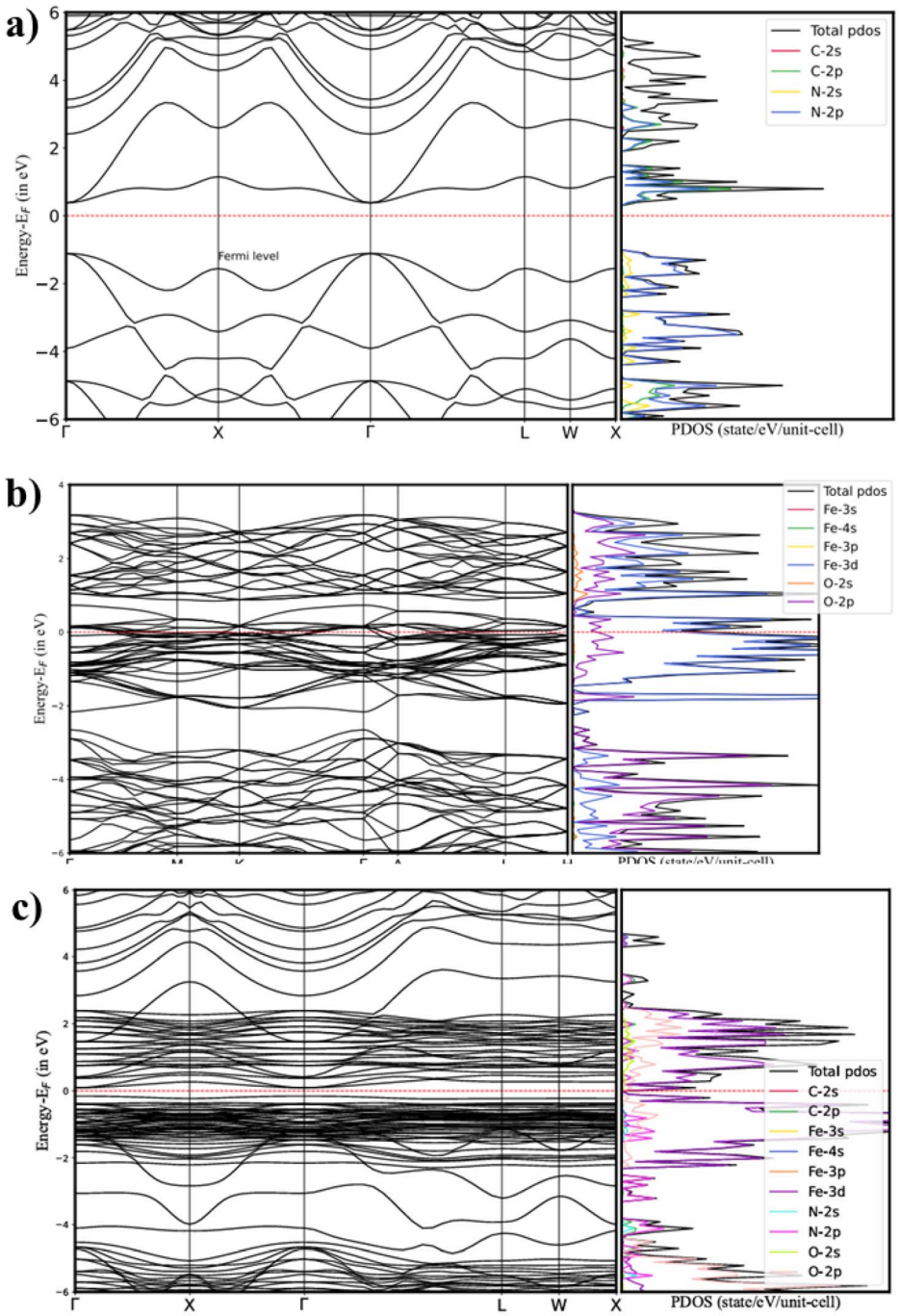

Fig. 9 Band structure and PDOS plots of g-C_3N_4 (a), α-Fe_2O_3 (b), and α-Fe_2O_3/g-C_3N_4 (c).

confirming the significant role of the leaf extract in facilitating controlled growth, enhancing surface properties, and improving the overall efficiency of the heterojunction.

3.10 Effect of FC 20 dosages

The effect of FC 20 dosage was systematically investigated in the range of 0.1 to 1.0 mg L^{-1}, keeping TCH concentration constant (20 mg L^{-1}), as presented in Fig. 10(b). The results showed that the extent of degradation was initially increased with an increase in catalyst dosage, achieving an optimal value. Beyond an optimal catalyst dose, further increases in FC 20 did not result in any significant improvements in degradation efficiency, which is due to the aggregation of FC 20 particles at higher dosages, leading to the onset of light scattering rather than light absorption.

3.11 Effect of TCH concentration

The influence of initial TCH concentration on its degradation using FC 20 is shown in Fig. 11(a). The photocatalytic efficacy decreased with increasing initial TCH concentration. At 10 and

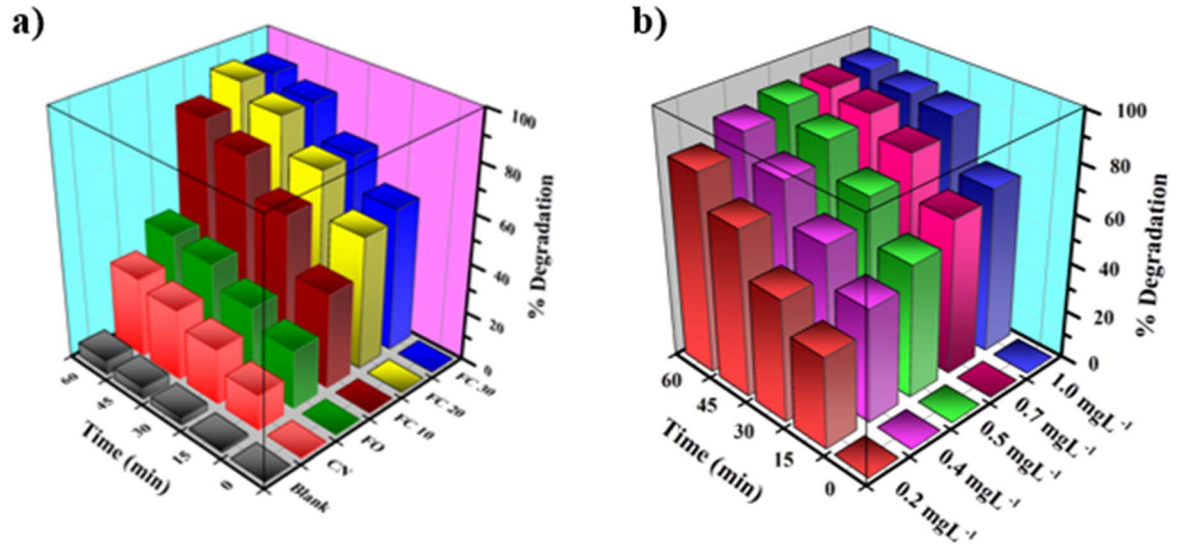

Fig. 10 Effect of different catalysts (a) and FC 20 dose (b) on the degradation efficiency of TCH.

20 mg L^{-1}, significant reductions in C/C_0 were observed, reaching approximately 0.08 value of C/C_0 after 60 min, demonstrating maximal degradation. However, the degradation efficiency decreased at higher concentrations (25 and 30 mg L^{-1}), with C/C_0 remaining around 0.2 and above 0.6, respectively. This decline can be attributed to the saturation of

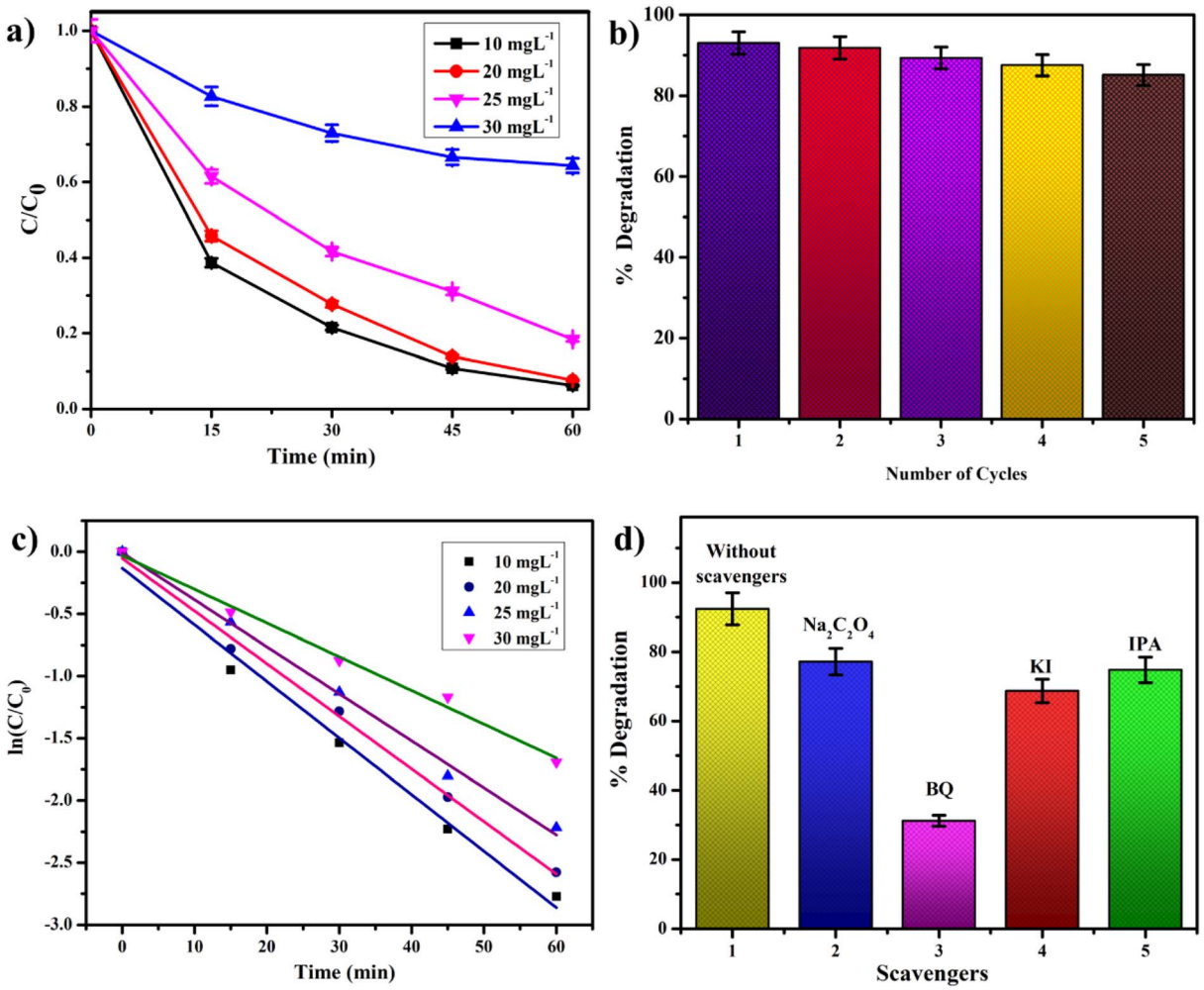

Fig. 11 Effect of TCH dose (a), recyclability test (b), kinetic study (c), and scavenging test (d) on the degradation efficiency.

reactive sites on FC 20 and the limited availability of reactive species to degrade TCH molecules. These results indicate that lower initial concentrations favor higher degradation rates due to the more effective interaction between the catalyst and the target molecules.

3.12 Effect of pH

The photocatalytic degradation efficiency of TCH by FC20 was evaluated under varying pH conditions (3.0–10.0) and is presented in Fig. S5 (ESI†). The removal rates were 74.3% at pH 3.0, increased to a maximum of 93% at pH 6.3, then slightly decreased at higher pH levels (84.5% at pH 8, and 78.9% at pH 10). This trend suggests that the initial pH of the solution has a significant impact on its photocatalytic activity. Zeta potential analysis showed a point of zero charge (PZC) at pH 5.72 (Fig. S6, ESI†), suggesting that the catalyst surface is positively charged at pH < 5.72 and negatively charged at pH > 5.72. TCH molecules exhibit different forms depending on pH, such as cationic (<3.3), zwitterionic (3.3–7.7), and anionic (>7.7).[61,62] At pH 3.0, repulsion between the positively charged surface and cationic TCH reduces degradation efficiency. At pH 10.0, both the catalyst and TC are negatively charged, again causing repulsion. Maximum degradation at pH 6–7 corresponds to the zwitterionic form of TCH, where electrostatic interactions are favorable. Overall, the α-Fe_2O_3/g-g-C_3N_4 catalyst shows stable performance over a wide pH range, with optimal activity under mildly acidic conditions.

3.13 Heterogeneity and recyclability

The test of heterogeneity of catalytic experiments remains of foremost importance. The catalytic reactions were run with the filtrate solution, which was obtained after washing the catalyst, and about 7% of degradation was achieved. The degradation obtained is nearly the same as that of the photolysis results. These results revealed that the photocatalytic degradation results from the heterogeneous FC 20 catalyst. Additionally, the Fe content in the filtrate was below the detection limit, confirming that no iron leaching occurred during the reaction. Degradation experiments were performed over regenerated catalysts for five consecutive runs to assess the reusability of the catalyst, as shown in Fig. 11(b). A marginal fall in catalytic efficiency (<8%) is well within the experimental error, demonstrating the excellent stability and reusability of the catalyst. The post-reaction characterization studies such as XRD and FT IR were carried out after the 5th cycle, and they showed almost similar spectra to those of the initially prepared samples (Fig. S7, ESI†).

3.14 Kinetic study

The catalytic degradation of TCH was investigated at initial concentrations of 10, 20, 25, and 30 mg L^{-1} to evaluate the kinetic behavior of the reaction. The experimental data were well fitted into the first-order kinetic model, represented by the equation:

$$\ln C_t = -kt + \ln C_0 \quad (2)$$

Table 2 Relationship between the TCH concentration and the rate constant

Sl. no.	TCH con. (mg L^{-1})	R^2	Rate constant (k, s^{-1})
1	10	0.989	0.0455
2	20	0.996	0.0423
3	25	0.995	0.0378
4	30	0.992	0.0271

$$\ln\left(\frac{C_t}{C_0}\right) = -kt \quad (3)$$

where C_0 is the initial concentration of TCH, C is the concentration of TCH at time t, and k is the apparent first-order rate constant (min^{-1}).

Fig. 11(c) presents the linear relationship between $\ln(C_0/C)$ and time for the different initial concentrations, confirming first-order kinetics with a high correlation coefficient ($R^2 \simeq 0.99$) for all concentrations. The slope of each line corresponds to the apparent first-order rate constant (k), which decreased slightly with increasing TCH concentration. This indicates a potential decrease in catalytic efficiency due to competitive adsorption of TCH molecules at higher concentrations. The rate constants derived from the linear fits are summarized in Table 2. The results were consistent and showed the first-order behavior across all concentrations.

3.15 Scavenging tests

The scavenging test provides critical insights into the reactive species involved in the photocatalytic reaction. Various types of scavengers, such as potassium iodide, isopropyl alcohol, benzoquinone, sodium oxalate, *etc.*, were employed to identify the effect of active species. Potassium iodide and isopropyl alcohol are well-known scavengers of hydroxyl radicals, whereas benzoquinone and sodium oxalate are used for the scavenging of superoxide radicals and holes, respectively. The addition of benzoquinone caused a pronounced reduction in efficiency to 30–40%, demonstrating that superoxide radicals are the dominant reactive species driving the degradation. Upon introduction of sodium oxalate, the degradation efficiency was decreased to 60–65% (Fig. 11(d)), highlighting the significant contribution of the hole to the degradation mechanism. Potassium iodide led to a moderate decrease in efficiency to approximately 70%. Similarly, isopropyl alcohol reduced the activity to 80%, indicating that hydroxyl radicals play a minor role. These results conclusively identify superoxide radicals as the dominant reactive species in the system, with photogenerated holes and hydroxyl radicals serving the less significant roles.

3.16 Intermediates and plausible degradation pathways of tetracycline hydrochloride

The intermediates formed during the degradation process were investigated using a liquid chromatograph mass spectrometer (LCMS), and the obtained mass spectrogram is presented in

Fig. S8 (ESI†). Functional groups having high electron density, such as double bonds, amines, and phenolic hydroxyls, are vulnerable to free radical attacks from the catalyst during photocatalysis.[63] Based on the intermediates, the degradation pathway of tetracycline hydrochloride was speculated in four fragmentation pathways, as shown in Scheme 2. TCH degradation follows multiple pathways, each involving distinct fragmentation mechanisms. In Pathway I, TCH undergoes ring opening, deamination, and dihydroxylation, forming fragment F1 (m/z = 300). Subsequent dealkylation and decarboxylation convert F1 into F2 (m/z = 244), followed by further dealkylation of methyl and ethyl groups to yield F3 (m/z = 188). F3 then undergoes additional ring opening and dealkylation, forming F4. In Pathway II, TCH undergoes photocatalytic loss of its most reactive functional groups while retaining its carbon backbone, producing fragment F5 (m/z = 290). Demethylation and reduction of F5 generate F6 (m/z = 260), ultimately forming the stable fragment F7 by the ring-opening reaction. In Pathway III, the process starts with hydroxyl group removal, followed by ring opening and dealkylation, resulting in the formation of F8 (m/z = 279), followed by deamination to produce F9 (m/z = 194). Further fragmentation of F9 yields F10 (m/z = 154) and F11 (m/z = 168), both of which decompose into F12 (m/z = 142). Pathway IV involves the formation of two key fragments, F13 (m/z = 214) and F14 (m/z = 99). Ultimately, all degradation pathways converge toward mineralization, producing CO_2, H_2O, and other small organic compounds.

3.17 Proposed S-scheme charge transfer mechanism

The S-scheme mechanism for the photocatalytic degradation of TCH involves the formation of a heterojunction between α-

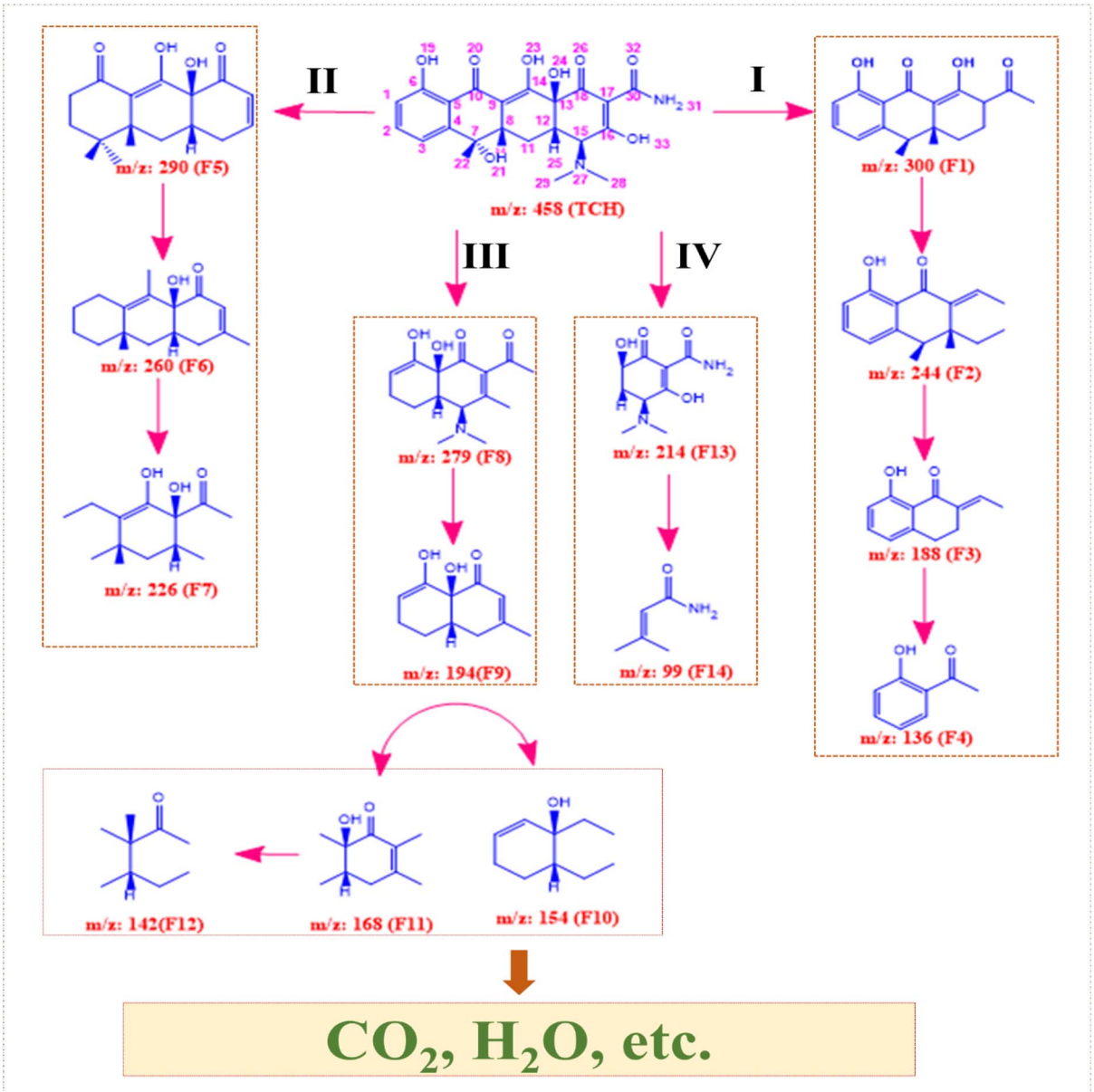

Scheme 2 Plausible degradation pathway of tetracycline hydrochloride.

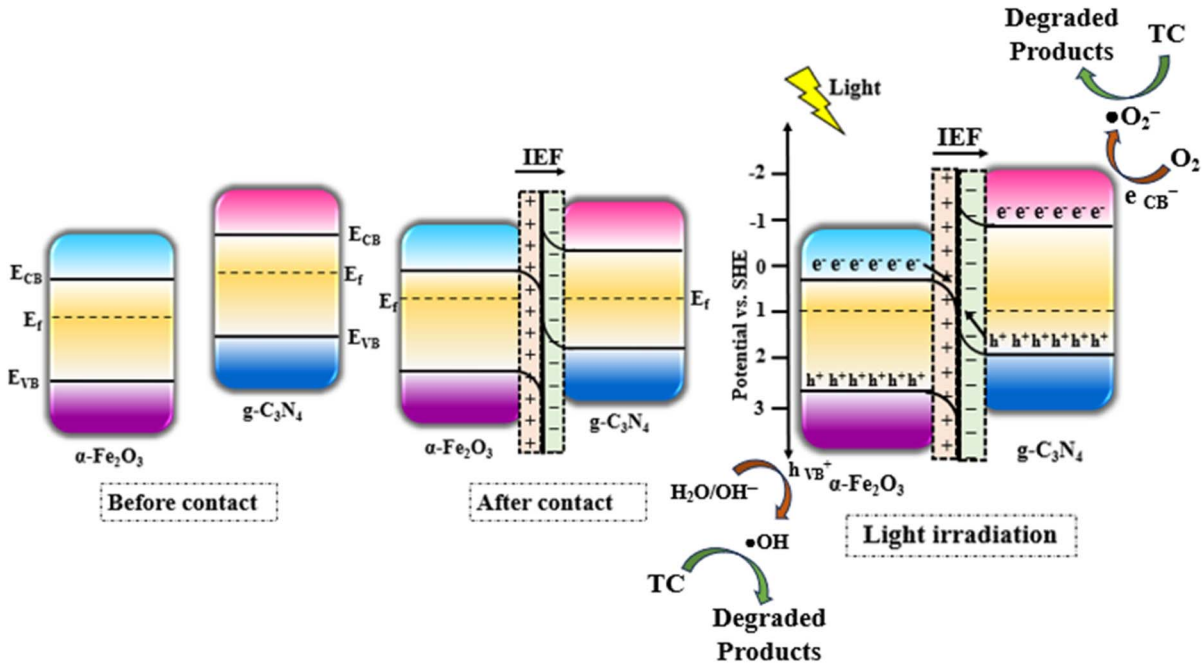

Scheme 3 Proposed S-scheme charge transfer mechanism in α-Fe_2O_3/g-C_3N_4.

Fe_2O_3 and g-C_3N_4, which is presented in Scheme 3. Before contact, the conduction band (CB) and valence band (VB) edges of the individual semiconductors are aligned with their respective Fermi levels (E_f). Upon forming a heterojunction, electron transfer occurs between the two materials until their Fermi levels equilibrate, generating an internal electric field (IEF) at the interface. Under light irradiation, α-Fe_2O_3 absorbs photons ($h\nu$), promoting electrons (e^-) from the VB to the CB and leaving photogenerated holes (h^+) in the VB. Simultaneously, photogenerated electrons from the CB of g-C_3N_4 transfer to the VB of α-Fe_2O_3 *via* the S-scheme pathway. This mechanism ensures the retention of highly oxidative holes in the VB of α-Fe_2O_3 and highly reductive electrons in the CB of g-C_3N_4. These charge carriers facilitate the production of reactive oxygen species (ROS), including superoxide ($\bullet O_2^-$) and hydroxyl ($\bullet OH$) radicals, which oxidize and degrade TCH into non-toxic products (Scheme 2). The S-scheme configuration, facilitated by the IEF, enhances charge separation and suppresses recombination, thereby improving photocatalytic efficiency.

$$\alpha\text{-}Fe_2O_3/g\text{-}C_3N_4 + h\nu \rightarrow \alpha\text{-}Fe_2O_3/g\text{-}C_3N_4(h_{VB}^+ + e_{CB}^-) \quad (4)$$

$$\alpha\text{-}Fe_2O_3/g\text{-}C_3N_4\ (h_{VB}^+ + e_{CB}^-) \rightarrow \text{S-Scheme } \alpha\text{-}Fe_2O_3\ (h_{VB}^+) + g\text{-}C_3N_4\ (e_{CB}^-) \quad (5)$$

$$\alpha\text{-}Fe_2O_3\ (h_{VB}^+) + H_2O \rightarrow \bullet OH + H^+ \quad (6)$$

$$g\text{-}C_3N_4\ (e_{CB}^-) + O_2 \rightarrow \bullet O_2^- \quad (7)$$

$$g\text{-}C_3N_4\ (e_{CB}^-) + \bullet O_2^- + 2H^+ \rightarrow H_2O_2 \quad (8)$$

$$g\text{-}C_3N_4\ (e_{CB}^-) + H_2O_2 + H^+ \rightarrow \bullet OH + H_2O \quad (9)$$

$$\text{Tetracycline hydrochloride} + \bullet OH + \bullet O_2^- \rightarrow CO_2 + H_2O + \text{small molecules} \quad (10)$$

4 Conclusion

The present investigation is a successful demonstration of utilizing a naturally occurring and underused renewable resource towards the sustainable development of photocatalysts. *Nyctanthes arbor-tristis* L. leaf extract can be employed as a templating agent towards the design of a cost-effective S-scheme based α-Fe_2O_3/g-C_3N_4 heterojunction photocatalyst for the efficient decontamination of TCH. Comprehensive structural and optical characterization confirmed the formation of the heterojunction, with good phase purity, distinct crystallinity, functional groups, and elemental composition. FESEM and HRTEM images showed uniform spherical morphologies of the catalyst. The optimized photocatalyst exhibited a tailored band gap of 2.2 eV, a high surface area of 21 $m^2\ g^{-1}$, and a significantly reduced recombination rate, making it highly effective for visible-light-driven photocatalysis. About ~93% of tetracycline hydrochloride degradation was achieved in the presence of FC 20 under visible light, substantially outperforming the activities of individual components, *i.e.*, 32% and 43% for g-C_3N_4 and α-Fe_2O_3, respectively. Mechanistic investigations confirmed that superoxide radicals ($\bullet O_2^-$) were the primary reactive species catalyzing the degradation of TCH. Density Functional Theory (DFT) calculations and differential charge density mapping further validated the S-scheme charge transfer mechanism, demonstrating the spatially resolved electron–hole separation. Based on experimental observations and fragmentation patterns observed from LCMS studies,

a plausible pathway for TCH degradation was presented. The findings provide valuable insights into the scalable development of sustainable materials for environmental remediation, particularly in wastewater treatment applications targeting persistent organic pollutants.

Data availability

The data supporting this article have been included as part of the ESI.†

Author contributions

Mano Ranjan Barik: investigation, methodology, software, writing – original draft, data curation. Sushanta Kumar Badamali: supervision, conceptualization, methodology, writing – review & editing, formal analysis. Jagadish Kumar: software, methodology, formal analysis.

Conflicts of interest

There are no conflicts to declare.

Acknowledgements

MB deeply acknowledges the Center of Advanced Materials and Applications, Dept. of Chemistry, Utkal University, for providing research facilities. MB is thankful to the Central Research Facility, KIIT University, for the XRD, FESEM, and LCMS analyses. MB also thanks the Material Analysis and Research Center, Bengaluru, for the BET analysis. MB gratefully acknowledges the University Grant Commission, Government of India, for the award of a Junior Research Fellowship to pursue doctoral work.

References

1 P. Gao, M. Munir and I. Xagoraraki, Correlation of tetracycline and sulfonamide antibiotics with corresponding resistance genes and resistant bacteria in a conventional municipal wastewater treatment plant, *Sci. Total Environ.*, 2012, **421**(1), 173–183.
2 C. V. Gómez-Pacheco, M. Sánchez-Polo, J. Rivera-Utrilla and J. López-Peñalver, Tetracycline removal from waters by integrated technologies based on ozonation and biodegradation, *Chem. Eng. J.*, 2011, **178**, 115–121.
3 G. Crini and E. Lichtfouse, Advantages and disadvantages of techniques used for wastewater treatment, *Environ. Chem. Lett.*, 2019, **17**, 145–155.
4 A. Fujishima and K. Honda, Electrochemical photolysis of water at a semiconductor electrode, *Nature*, 1972, **238**(5358), 37–38.
5 K. Bisaria, S. Sinha, R. Singh and H. M. Iqbal, Recent advances in structural modifications of photo-catalysts for organic pollutants degradation–a comprehensive review, *Chemosphere*, 2021, **284**, 131263.
6 D. Chen, Y. Cheng, N. Zhou, P. Chen, Y. Wang, K. Li and R. Ruan, Photocatalytic degradation of organic pollutants using TiO_2-based photocatalysts: a review, *J. Clean. Prod.*, 2020, **268**, 121725.
7 J. Theerthagiri, S. Chandrasekaran, S. Salla, V. Elakkiya, R. A. Senthil, P. Nithyadharseni and H. S. Kim, Recent developments of metal oxide-based heterostructures for photocatalytic applications towards environmental remediation, *J. Solid State Chem.*, 2018, **267**, 35–52.
8 T. Velempini, E. Prabakaran and K. Pillay, Recent developments in the use of metal oxides for photocatalytic degradation of pharmaceutical pollutants in water—a review, *Mater. Today Chem.*, 2021, **19**, 100380.
9 S. Saida, D. K. Gorai and T. K. Kundu, A green process for the synthesis of porous TiO_2 from ilmenite ore using molten salt alkali decomposition for photocatalytic applications, *RSC Sustain.*, 2023, **1**(3), 592–598.
10 J. Ke, M. Adnan Younis, Y. Kong, H. Zhou, J. Liu, L. Lei and Y. Hou, Nanostructured ternary metal tungstate-based photocatalysts for environmental purification and solar water splitting: a review, *Nano-Micro Lett.*, 2018, **10**, 1–27.
11 Y. Sun, C. Wang, G. Gu, Y. Ma, Z. Xiong and Y. Liu, Facile synthesis of free-metal ternary composites for ultra-fast photocatalytic degradation of organic pollutant, *Catal. Today*, 2020, **340**, 294–301.
12 S. Bagheri, A. Termeh Yousefi and T. O. Do, Photocatalytic pathway toward degradation of environmental pharmaceutical pollutants: structure, kinetics and mechanism approach, *Catal. Sci. Technol.*, 2017, **7**(20), 4548–4569.
13 P. Zhang, Y. Jin, M. Li, X. Wang and Y. N. Zhang, Dual heterojunction-based $Au@TiO_2$ photoelectrode exhibiting efficient charge separation for enhanced removal of organic dye under visible light, *RSC Sustain.*, 2023, **1**(3), 622–630.
14 Q. Xu, L. Zhang, J. Yu, S. Wageh, A. A. Al-Ghamdi and M. Jaroniec, Direct Z-scheme photocatalysts: principles, synthesis, and applications, *Mater. Today*, 2018, **21**(10), 1042–1063.
15 J. Fu, Q. Xu, J. Low, C. Jiang and J. Yu, Ultrathin 2D/2D WO_3/g-C_3N_4 step-scheme H_2-production photocatalyst, *Appl. Catal., B*, 2019, **243**, 556–565.
16 B. Zhang, H. Shi, Y. Yan, C. Liu, X. Hu, E. Liu and J. Fan, A novel S-scheme 1D/2D Bi_2S_3/g-C_3N_4 heterojunction with enhanced H_2 evolution activity, *Colloids Surf., A*, 2021, **608**, 125598.
17 H. Yang, D. He, C. Liu, T. Zhang, J. Qu, D. Jin and Y. N. Zhang, Visible-light-driven photocatalytic disinfection by S-scheme α-Fe_2O_3/g-C_3N_4 heterojunction: bactericidal performance and mechanism insight, *Chemosphere*, 2022, **287**, 132072.
18 Q. Xu, L. Zhang, B. Cheng, J. Fan and J. Yu, S-scheme heterojunction photocatalyst, *Chem*, 2020, **6**(7), 1543–1559.
19 Y. Li, Z. Xia, Q. Yang, L. Wang and Y. Xing, Review on g-C_3N_4-based S-scheme heterojunction photocatalysts, *J. Mater. Sci. Technol.*, 2022, **125**, 128–144.
20 A. J. Deotale and R. V. Nandedkar, Correlation between particle size, strain and band gap of iron oxide nanoparticles, *Mater. Today: Proc.*, 2016, **3**(6), 2069–2076.

21 K. Maeda, X. Wang, Y. Nishihara, D. Lu, M. Antonietti and K. Domen, Photocatalytic activities of graphitic carbon nitride powder for water reduction and oxidation under visible light, *J. Phys. Chem. C*, 2009, **113**(12), 4940–4947.
22 Z. Zhao, Y. Sun and F. Dong, Graphitic carbon nitride-based nanocomposites: a review, *Nanoscale*, 2015, **7**(1), 15–37.
23 M. Y. Akram, T. Ashraf, L. Tong, X. Yin, H. Dong and H. Lu, Architecting high-performance photocatalysts: a review of modified 2D/2D graphene/g-C_3N_4 heterostructures, *J. Environ. Chem. Eng.*, 2024, 113415.
24 D. Bhanderi, P. Lakhani and C. K. Modi, Graphitic carbon nitride (g-C_3N_4) as an emerging photocatalyst for sustainable environmental applications: a comprehensive review, *RSC Sustain.*, 2024, **2**(2), 265–287.
25 Y. Li, S. Zhu, Y. Liang, Z. Li, S. Wu, C. Chang and Z. Cui, Synthesis of α-Fe_2O_3/g-C_3N_4 photocatalyst for high-efficiency water splitting under full light, *Mater. Des.*, 2020, **196**, 109191.
26 B. Palanivel, M. S. Hossain, M. S. Raghu, K. Y. Kumar, R. R. Macadangdang Jr, M. Ubaidullah and S. H. Park, Green synthesis of Fe_2O_3 deposited g-C_3N_4: addition of rGO promoted Z-scheme ternary heterojunction for efficient photocatalytic degradation and H_2 evolution reaction, *Mater. Res. Bull.*, 2023, **162**, 112177.
27 M. Sundrarajan and S. Gowri, Green synthesis of titanium dioxide nanoparticles by *Nyctanthes arbor-tristis* leaves extract, *Chalcogenide Lett.*, 2011, **8**(8), 447–451.
28 G. Cao, E. Sofic and R. L. Prior, Antioxidant capacity of tea and common vegetables, *J. Agric. Food Chem.*, 1996, **44**, 3426–3431.
29 Y. Velioglu, G. Mazza, L. Gao and B. D. Oomah, Antioxidant activity and total phenolics in selected fruits, vegetables, and grain products, *J. Agric. Food Chem.*, 1998, **46**(10), 4113–4117.
30 X. Liao, T. T. Li, H. T. Ren, Z. Mao, X. Zhang, J. H. Lin and C. W. Lou, Enhanced photocatalytic performance through the ferroelectric synergistic effect of pn heterojunction $BiFeO_3/TiO_2$ under visible-light irradiation, *Ceram. Int.*, 2021, **47**(8), 10786–10795.
31 D. Chen, S. Wu, J. Fang, S. Lu, G. Zhou, W. Feng and Z. Fang, A nanosheet-like α-Bi_2O_3/g-C_3N_4 heterostructure modified by plasmonic metallic Bi and oxygen vacancies with high photodegradation activity of organic pollutants, *Sep. Purif. Technol.*, 2018, **193**, 232–241.
32 C. Li, S. Yu, H. Che, X. Zhang, J. Han, Y. Mao and H. Dong, Fabrication of Z-scheme heterojunction by anchoring mesoporous γ-Fe_2O_3 nanospheres on g-C_3N_4 for degrading tetracycline hydrochloride in water, *ACS Sustainable Chem. Eng.*, 2018, **6**(12), 16437–16447.
33 F. Guo, W. Shi, M. Li, Y. Shi and H. Wen, 2D/2D Z-scheme heterojunction of $CuInS_2$/g-C_3N_4 for enhanced visible-light-driven photocatalytic activity towards the degradation of tetracycline, *Sep. Purif. Technol.*, 2019, **210**, 608–615.
34 F. Guo, W. Shi, H. Wang, H. Huang, Y. Liu and Z. Kang, Fabrication of a $CuBi_2O_4$/g-C_3N_4 p–n heterojunction with enhanced visible light photocatalytic efficiency toward tetracycline degradation, *Inorg. Chem. Front.*, 2017, **4**(10), 1714–1720.
35 D. Li, F. Shi, D. Jiang, M. Chen and W. Shi, $CdIn_2S_4$/g-C_3N_4 heterojunction photocatalysts: enhanced photocatalytic performance and charge transfer mechanism, *RSC Adv.*, 2017, **7**(1), 231–237.
36 Y. Hong, C. Li, G. Zhang, Y. Meng, B. Yin, Y. Zhao and W. Shi, Efficient and stable Nb_2O_5 modified g-C_3N_4 photocatalyst for removal of antibiotic pollutant, *Chem. Eng. J.*, 2016, **299**, 74–84.
37 D. E. Christy, E. Vijayakumar, A. J. Bosco and P. M. Johnson, Dahlia flower-like layered α-MnO_2/B@g-C_3N_4 nanocomposite for visible light-induced photocatalytic removal of tetracycline, *Opt. Mater.*, 2023, **136**, 113429.
38 S. Zhao, F. Chen, Y. Song, J. Hua, R. Wu, J. Yang and Y. Tang, Boosted degradation of tetracycline over a novel hierarchical 2D/1D S-scheme heterojunction Bi_2O_4@SnS under visible light irradiation, *J. Environ. Chem. Eng.*, 2023, **11**(2), 109262.
39 J. Jiang, S. Zhao, C. Zhang, F. Chen, Y. Song and Y. Tang, Construction of S-scheme heterojunction WO_3/Bi_2O_4 with significantly enhanced visible-light-driven activity for degradation of tetracycline, *J. Environ. Chem. Eng.*, 2023, **11**(5), 110685.
40 W. Wang, Z. Li, H. Wang, H. Luo, Z. Meng, X. Liu and Q. He, Construction of novel dual Z-scheme g-C_3N_4/$ZnFe_2O_4$/Ag_2CO_3 heterojunction with enhanced visible-light-driven performance for tetracycline degradation and bacterial inactivation, *J. Environ. Chem. Eng.*, 2023, **11**(6), 111421.
41 M. Azqandi, K. Nateq, M. Amarzadeh, M. Yoosefian, A. Yaghoot-Nezhad, A. Ahmad and N. Nasseh, Intensified photo-decontamination of tetracycline antibiotic by S-scheme spinel manganese ferrite-grafted ZIF-8 heterojunction photocatalyst: mechanism conception, degradation pathway and DFT studies, *J. Environ. Chem. Eng.*, 2024, **12**(3), 112875.
42 J. Liu, W. Yuan, M. Zhu, S. Ganesan, N. I. Vatin, D. Zhang and X. Liu, Construction of $Mn_{0.3}Cd_{0.7}S$/$FeNi_8$-LDH S-scheme heterojunction for enhanced photocatalytic degradation of tetracycline under visible light, *J. Environ. Chem. Eng.*, 2024, **12**(3), 112944.
43 Y. Wei, Y. B. Liu, C. Liu, X. Li, G. H. Zhao, R. H. Liu, et al., Construction of oxygen-doped g-C_3N_4/BiOCl (S-scheme) heterojunction: efficient degradation of tetracycline in wastewater, *J. Environ. Chem. Eng.*, 2024, **12**, 113354.
44 Y. Zhang, J. Liu, G. Wu and W. Chen, Porous graphitic carbon nitride synthesized via direct polymerization of urea for efficient sunlight-driven photocatalytic hydrogen production, *Nanoscale*, 2012, **4**, 5300–5303.
45 S. Lenka and S. K. Badamali, Nanostructured ZnO as an efficient heterogeneous photocatalyst towards degradation of lignin under visible light irradiation, *Mol. Catal.*, 2023, **536**, 112918.
46 F. Guo, W. Shi, H. Wang, H. Huang, Y. Liu and Z. Kang, Fabrication of a $CuBi_2O_4$/g-C_3N_4 p–n heterojunction with enhanced visible light photocatalytic efficiency toward tetracycline degradation, *Inorg. Chem. Front.*, 2017, **4**, 1714–1720.
47 H. Cui, Y. Liu and W. Ren, Structure switch between α-Fe_2O_3, γ-Fe_2O_3 and Fe_3O_4 during the large scale and low

temperature sol–gel synthesis of nearly monodispersed iron oxide nanoparticles, *Adv. Powder Technol.*, 2013, **24**, 93–97.
48 Y. Zhang, J. Liu, G. Wu and W. Chen, Porous graphitic carbon nitride synthesized via direct polymerization of urea for efficient sunlight-driven photocatalytic hydrogen production, *Nanoscale*, 2012, **4**, 5300–5303.
49 O. Alduhaish, M. Ubaidullah, A. M. Al-Enizi, N. Alhokbany, S. M. Alshehri and J. Ahmed, Facile synthesis of mesoporous α-Fe_2O_3@g-C_3N_4-NCs for efficient bifunctional electro-catalytic activity (OER/ORR), *Sci. Rep.*, 2019, **9**, 14139.
50 S. Kang, J. Jang, R. C. Pawar, S. H. Ahn and C. S. Lee, Low temperature fabrication of Fe_2O_3 nanorod film coated with ultra-thin g-C_3N_4 for a direct z-scheme exerting photocatalytic activities, *RSC Adv.*, 2018, **8**, 33600–33613.
51 S. Babar, N. Gavade, H. Shinde, P. Mahajan, K. H. Lee, N. Mane, et al., Evolution of waste iron rust into magnetically separable g-C_3N_4–Fe_2O_3 photocatalyst: an efficient and economical waste management approach, *ACS Appl. Nano Mater.*, 2018, **1**, 4682–4694.
52 P. Giannozzi, S. Baroni, N. Bonini, M. Calandra, R. Car, C. Cavazzoni, et al., QUANTUM ESPRESSO: a modular and open-source software project for quantum simulations of materials, *J. Phys.: Condens. Matter*, 2009, **21**, 395502.
53 D. Vanderbilt, Soft self-consistent pseudopotentials in a generalized eigenvalue formalism, *Phys. Rev. B:Condens. Matter Mater. Phys.*, 1990, **41**, 7892.
54 J. P. Perdew, K. Burke and M. Ernzerhof, Generalized gradient approximation made simple, *Phys. Rev. Lett.*, 1996, **77**, 3865.
55 H. J. Monkhorst and J. D. Pack, Special points for Brillouin-zone integrations, *Phys. Rev. B:Condens. Matter Mater. Phys.*, 1976, **13**, 5188.
56 C. G. Broyden, The convergence of a class of double-rank minimization algorithms: 2. The new algorithm, *IMA J. Appl. Math.*, 1970, **6**, 222–231.
57 R. Fletcher, A new approach to variable metric algorithms, *Comput. J.*, 1970, **13**, 317–322.
58 D. Goldfarb, A family of variable-metric methods derived by variational means, *Math. Comput.*, 1970, **24**, 23–26.
59 D. F. Shanno, On variable metric methods for sparse Hessians, *Math. Comput.*, 1970, **24**, 647–657.
60 B. Wu, J. Wu, J. Li, Z. Qiao, P. Shen, Q. Zhang and Y. Ling, *Chem. Eng. J.*, 2023, **471**, 144575.
61 C. Wang, R. Sun, R. Huang and H. Wang, *Sep. Purif. Technol.*, 2021, **270**, 118773.
62 S. Kumari, A. Chowdhury, A. A. Khan and S. Hussain, *J. Hazard. Mater.*, 2021, **415**, 125750.
63 K. Shi, J. Wang, L. Yin, Y. Xu, D. Kong, H. Li, et al., Photocatalysis combined with microalgae to promote the degradation and detoxification of tetracycline hydrochloride, *Bull. Environ. Contam. Toxicol.*, 2023, **110**, 43.